DEFENSE TECHNICAL INFORMATION CENTER

Information for the Defense Community

DTIC® has determined on _8 /12 /2010_ that this Technical Document has the Distribution Statement checked below. The current distribution for this document can be found in the DTIC® Technical Report Database.

☒ **DISTRIBUTION STATEMENT A.** Approved for public release; distribution is unlimited. per ARL\SEDD

☐ **© COPYRIGHTED**; U.S. Government or Federal Rights License. All other rights and uses except those permitted by copyright law are reserved by the copyright owner.

☐ **DISTRIBUTION STATEMENT B.** Distribution authorized to U.S. Government agencies only (fill in reason) (date of determination). Other requests for this document shall be referred to (insert controlling DoD office)

☐ **DISTRIBUTION STATEMENT C.** Distribution authorized to U.S. Government Agencies and their contractors (fill in reason) (date of determination). Other requests for this document shall be referred to (insert controlling DoD office)

☐ **DISTRIBUTION STATEMENT D.** Distribution authorized to the Department of Defense and U.S. DoD contractors only (fill in reason) (date of determination). Other requests shall be referred to (insert controlling DoD office).

☐ **DISTRIBUTION STATEMENT E.** Distribution authorized to DoD Components only (fill in reason) (date of determination). Other requests shall be referred to (insert controlling DoD office).

☐ **DISTRIBUTION STATEMENT F.** Further dissemination only as directed by (inserting controlling DoD office) (date of determination) or higher DoD authority.

Distribution Statement F is also used when a document does not contain a distribution statement and no distribution statement can be determined.

☐ **DISTRIBUTION STATEMENT X.** Distribution authorized to U.S. Government Agencies and private individuals or enterprises eligible to obtain export-controlled technical data in accordance with DoDD 5230.25; (date of determination). DoD Controlling Office is (insert controlling DoD office).

Final Report

Contract # Number: W911NF-07-2-0048

Program Title :
MANUFACTURING TECHNOLOGY DEVELOPMENT OF ADVANCED COMPONENTS FOR
HIGH POWER SOLID STATE LASERS

Prime Contractor :

Onyx Optics, Inc.
6551 Sierra Lane
Dublin, Ca 94568
www.onyxoptics.com

ONYXOptics,Inc.

Program Manager :

Helmuth Meissner
Onyx Optics, Inc.
6551 Sierra Lane
Dublin, CA 94568
Email: hmeissner@onyxoptics.com
Ph: 925-833-1969
Fax: 925-833-1759

Document Preparation Date :   07-19-2010

20100722156

ONYX OPTICS, INC.

Final Report, July 2010

Title of Program:
Manufacturing Technology Development of Advanced Components for
High Power Solid State Lasers

1 Overview

The program has been successful in reaching the objective of developing a unique technology of Adhesive-Free Bond (AFB®) composite crystals, optical ceramics, glasses and optical coatings. Major highlights of the program include:

- AFB Nd:YAG/YAG composite slabs with undoped ends have enabled 100kW weapons level HEL (High Energy Lasers) through Onyx Optics manufacturing development.

- AFB Passive q-switched microchips are in advanced development for Sidewinder missiles.

- AFB Waveguide structures are in advanced development for a number of defense applications, with components of different sizes.

- AFB Disk laser components are used in production laser machining systems.

- AFB Nonlinear walk-off corrected crystal composites enable quasi-noncritical phase matching at any wavelengths that previously have only been accessible by critical phase matching and are relevant for infrared countermeasures (IRCM) and directed IRCM.

- AFB Ho:YAG lasers have been designed and developed that exhibit the best beam quality and highest efficiency of any that have been reported in the literature.

- AFB sapphire and ceramic spinel window development originating under this program has resulted in one phase II sbir and one phase II sbir subcontract.

- Optical, mechanical and thermal properties of AFB composites have been characterized that have placed the technology on a solid data basis for design of composite components and scale up to production.

- The program has enabled industry-wide scale-up of AFB® composite crystal components for solid state lasers that are concurrently being scaled up to prototype and production quantities at laser manufacturer and systems integrator facilities for wavelengths from the ultraviolet to the terahertz region. The customer base is world-wide.

1. Pilot production of AFB® laser components

1.1. Large composite slabs - Process research

We have developed a process that allows the fabrication of composite slabs consisting of planar waveguiding structures of ceramic or single crystal YAG and phosphate laser glass where their length dimension is principally limited by processing equipment. While some of the fixturing is not yet in place, we have in operation finishing equipment that will become capable of producing 0.75 meter long composite slabs. Scale-up to finishing equipment with even larger component size and length capabilities has been defined.

1.2. Manufacture of flexible waveguides

The AFB fabrication of double clad planar and single core flexible waveguides follows a process that already has been developed at Onyx Optics for crystalline waveguides, with the only difference being that the outer cladding layers are thinner. The outer cladding has consisted of either sapphire or ceramic spinel both of which are very compatible with single crystal or ceramic YAG. Free-standing 200 mm x 10 mm x 47 μm thick undoped YAG slabs have been demonstrated to be manufacturable and flexible (Fig.1.1).
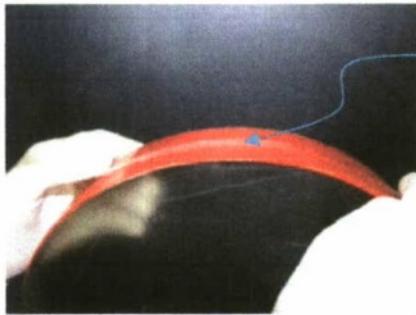

Fig. 1.1 Flexible YAG strip of 200x10x0.047 mm3, bent over 300mm diameter.

2. Property characterization of AFB components

2.1. Refractive index difference between doped and undoped YAG composites

Waveguide design requires precise refractive index data of the core and of the claddings. When the core is rare earth ion doped YAG and the cladding layers are the undoped YAG, we need to know the refractive index difference between the two. The refractive index of rare earth ion doped YAG depends also on the dopant concentration and can be characterized by the specific refractive index variation, $\Delta n/c$, with the unit of [/1%].

We have developed a refractive index difference measurement technique that implements both the MST technology of Zygo wavelength shift interferometer (VeriFire) for optical path distance measurement and the AFB technology for YAG sample preparation. The

technique allows resolution of refractive index differences being limited only by the physical thickness measurement of the samples.

Two doublet samples in which the geometry and the dimension are shown in **Figure 2.1** below validate the technique and give information on resolvable range of refractive index difference for a given thickness of the samples for further optimization of data acquisition.

(a) 10.07(L) x 24.91 (W) x 5.10(T)   (b) 9.96(L) x 10.01(W) x 5.04(T)
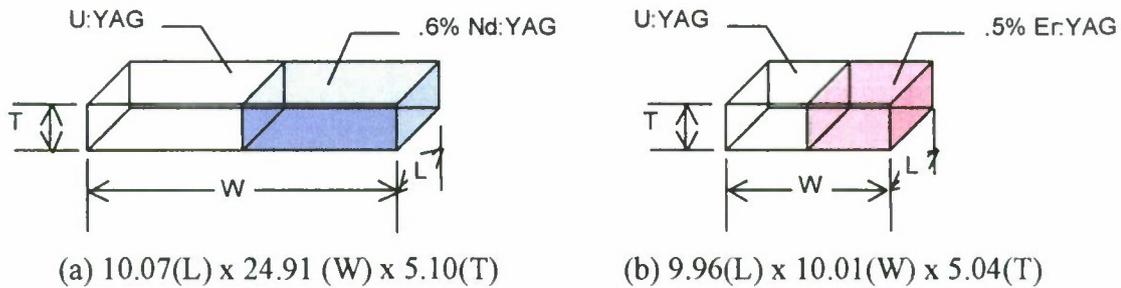
Figure 2.1. AFB composite samples for difference refractive index measurements.

By placing the AFB component in the null measuring cavity of the VeriFire (as shown in **Figure 2.2**), one can map the optical path distance distribution near the interface region. An oblique angle may be used to resolve the order of fringes between the two sections as shown in **Figure 2.3**. Since the technique is very sensitive, the proper thickness of the sample may be calculated before fabrication.
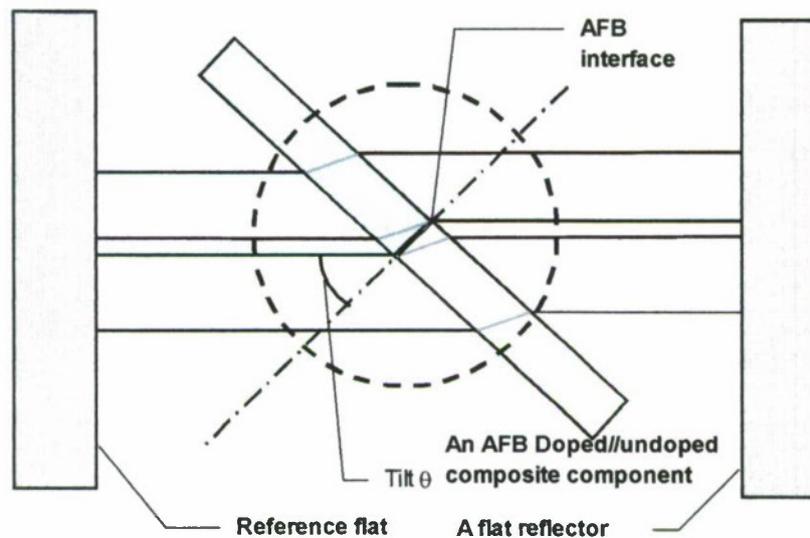
Figure 2.2. The null cavity setup and the schematics of optical path distances of a rotated sample about the vertical axis.

The resultant interferograms of three measured samples are shown in **Figure 7**.

(A) .6% Nd:YAG: UYAG #1   (B) 5% Er:YAG: UYAG #1

Figure 2.3. Typical fringe patterns of a .6% Nd:YAG// undoped YAG (U:YAG) composite of a 62° incident angle in (A), and a .5% Er:YAG// U:YAG composite of a 20° incident angle in (B)

The refractive index difference between 0.6%Nd:YAG and U:YAG has been further estimated by measuring the difference in optical distances (ΔOPD) across the AFB interfaces of two 0.6% Nd:YAG // U:YAG composites at various incident angles (θ).

The resultant ΔOPD data are plotted against the angle θ as shown in **Figure 2.4(A)** below.

The refractive index difference between .5%Er:YAG and U:YAG has been also estimated by measuring the difference in optical distances (ΔOPD) across the AFB interfaces of two .5% Er:YAG // U:YAG composites in various incident angles (θ).The resultant ΔOPD data are plotted against the angle θ as shown in **Figure 2.4(B)** below.
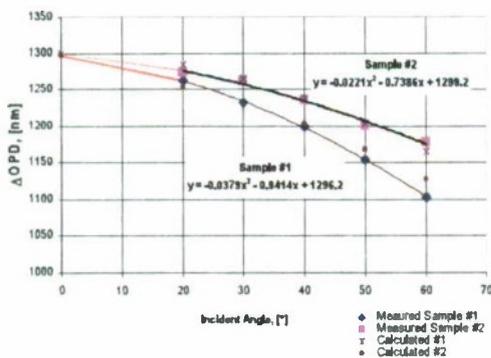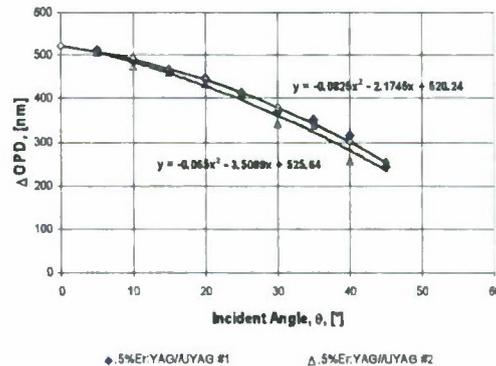
(A)   (B)

Figure 2.4. The difference in optical path distance between .6%Nd:YAG and undoped YAG of two composite samples is plotted as a function of the incident angle θ in (A), and the difference in optical path distance between .5%Er:YAG and undoped YAG of two composite samples is plotted as a function of the incident angle θ in (B).

The technique allows extrapolation of the polynomial fit experimental data to the difference in optical path distance at normal incidence that cannot be directly measured

due to the multiple orders of offsets in fringes. We have found the ΔOPD of the samples of the same dopant type and concentration converges to a unique value that gives an accurate estimation of the difference in refractive index between two YAG components.

The difference in optical path distance can be written as a function of the rotation angle θ by the following equation. $\Delta OPD(\theta) = \Delta OPD(0) - \Delta n*(d_1 - d_2)$, where θ = rotation angle, d_1 (the physical path length in component 1) = $t/\cos(\sin^{-1}(\sin(\theta)/n_2)$, $d1 = t/\cos(\sin^{-1}(\sin(\theta)/n_1)$, $\Delta n = n_2 - n_1 = \Delta OPD(0)/(2*t)$, where t = thickness of the component, n_1 is the refractive index of undoped YAG and is given by the Sellmeier equation. The calculated results fit well with the experimental data as shown in plots in **Figure 2.4**.

The calculated refractive index difference between 0.6% Nd:YAG and U:YAG is 2.53 x 10^{-4} and the specific refractive index variation is 4.22 x 10^{-4} per 1% Nd dopant concentration. The calculated refractive index difference between .5% Er:YAG and U:YAG is 1.04 x 10^{-4} and the specific refractive index variation is 2.08 x 10^{-4} per 1% Er dopant concentration.

2.2. Fracture toughness of YAG composites

We have measured the fracture toughness as it is related to the fracture strength when different orientations of YAG single crystals are bonded to each other to make a selection of a mechanically desirable waveguide configuration.

A functional waveguide contains multilayer structures that can be fabricated with AFB technology. The AFB YAG layers of different orientations, of different dopant type and of different dopant levels are of critical interest for lasing host component design. We have measured the fracture toughness of AFB composites of different bonding configurations. We have prepared YAG//YAG composite samples of (110)//(110), (211)//(211) bonding planes, and (111) twist twin and (111) flip twin composites. The measured data are compared to the measured control samples.

The configurations of the composite group contain three types, namely, conforming twin, twist twin and the flip twin. A conforming twin is formed by joining two YAG sections of the same crystallographic orientation via an AFB interface. A twist 180° twins is formed by joining two YAG sections of the same orientation except they are relatively rotated by 180° about the z directions. The flip twins are more complicated. For tetragonal components in a Cartesian coordinate, a flip twin is formed by joining two YAG sections of the opposite orientations by a relative rotation of 180° either about the x-axis to form the x-flip type or about the y-axis to form the y-flip type.

For the given size and the geometry of a notch made by a laser marking process and aligned with the loading direction, one can find the apparent fracture toughness of an AFB composite bar using the standard four point bending method. If the notch coincides with the bonded interface at the edges under a uniform tensile load (L_f) and if the test component delaminates during a four point bending test, one can consider that the maximum tensile failure load (σ_f) is the stress that balances the attractive potential (A_{vdw}) induced by the Van der Waals attractions.

We consider the delaminating interface of an AFB composite being the equivalent to the propagating crack that leads to fracture failure according to the Griffith theory. The fracture toughness, K_{IC}, characterizes the resistance of a solid material against the fracture failure upon an external tensile load that is locally intensified by the surface flaws to the magnitude surpassing the bonding force and consequently leading to unstable crack propagation to failure. The fracture toughness can be calculated by the following equation.

$$K_{IC} = 1.12 * \sigma_f * \sqrt{(\pi * a)} \quad \textbf{Eq. 1}$$

Where $\sigma_f =$ the apparent tensile breaking strength and is given by the equation **Eq. 2** below, and **a** = the size of the failing flaw that is measured experimentally.

$$\sigma_f = (3/2) * L_f * (S_s - L_s)/(w * t^2) \qquad \textbf{Eq. 2}$$

where L_f = the measured failing load, S_s = the support span, L_s = the load span, w = the width of the bar, and t = the thickness of the bar.

Both delamination of AFB interface and crack propagation in bulk share the same phenomenon of generating two new surfaces. The former regenerates the two initial surfaces that are bonded by London-Van der Waals forces, and the later generates the severed surfaces from the bulk that are held together by chemical bonds. The energy required to produce the two surfaces correlates to the force held the as separated two surfaces together in the first place. By using the fracture test, we can correlate the bond energy to the fracture toughness given the apparent tensile breaking stress and the initial well defined flaw size. The correlation between the two is shown in **Eq. 3** below.

$$G_{IC} = (1 - \upsilon^2) * K_{IC}^2 / E \qquad \textbf{Eq. 3}$$

where G_{IC} = the specific strain energy for fracture, $[J/m^2]$, υ = Poisson's ratio, E = the Young's modulus. We can then convert the **K_{IC}** data obtained from experiments to the bonding energy data.

We already know that the (211) plane of YAG can be polished to a smoother surface than (110). We have prepared two sets of conforming twins; one bonds in (110) planes and the other bonds in (211) planes.
The average fracture toughness of (211) conforming twins has been found to be 24% greater than that of (110) conforming twins.

We assume that the surface micro-roughness of AFB bonding surfaces plays a critical role in attaining the equilibrium separation distance between two bonding members. Given the same fabrication process, we may find correlation between the equilibrium surface roughness and the crystallographic orientations of the polished surfaces. The three common orientations of the bonding surfaces are the (111), (110), and (211) planes.

We have found that the average rms roughness of (110) bonding plane is 2.62 ± .41 Å, of (211) bonding plane is 2.34 ± .20 Å, and of (111) bonding plane is 2.56 ± .11 Å.

2.3. Interferometric method for measuring thermal conductivity and heat transfer of composite components

This technique has been developed to measure the thermal conductivity of non-composites and composites as function of temperature between cryogenic temperatures and about 300° C. It has established that AFB composites have no resistance in heat transfer at the interface.

2.3.1. Theoretical background

An increase of crystal temperature will cause a thermal expansion and refractive index change. The overall effect is reflected by the optical length change of the crystal that can be written as:

$$nL = (n_0 + \frac{dn}{dt}\Delta T) \cdot (L_0 + L_0 \cdot \alpha \cdot \Delta T) \qquad (1)$$

$$\Delta nL = L_0(n_0 \cdot \alpha + \frac{dn}{dt})\Delta T + L_0 \cdot \alpha \cdot \frac{dn}{dt} \cdot \Delta T^2 \qquad (2)$$

where, α is the thermal coefficient of expansion, dn/dt is the temperature derivative of the refractive indices.

Since both α and dn/dt are much smaller than 1 (for YAG crystal, $\alpha \sim 7.7 \times 10^{-6}$, dn/dt $\sim$ 8.9×10^{-6}), the second term on the right side of Eq. (2) will be negligible if the temperature is not too high. Under this approximation, the change of crystal optical length will be proportional to the crystal temperature change.

$$\Delta nL = L_0(n_0 \cdot \alpha + \frac{dn}{dt})\Delta T = L_0 \gamma \Delta T \qquad (3)$$

where we define γ as an overall thermal expansion coefficient of the crystal optical length.

Now let's consider a uniform rectangular crystal that has one end at a uniform temperature T and the opposite end at uniform temperature T+ΔT, the temperature gradient between these two ends will be linear:

$$\Delta T = \frac{Q \cdot L}{K \cdot S} \qquad (4)$$

Where, Q is the heat flow power, K is thermal conductivity, S is crystal cross section and L is the crystal length.

In this condition, the crystal would normally curve in the arc of a circle as shown in Fig. 1. The radius will be:

$$R = \frac{d}{\Delta T \cdot \alpha} \qquad (5)$$

Where, d is the width of the crystal between the hot and cold ends.
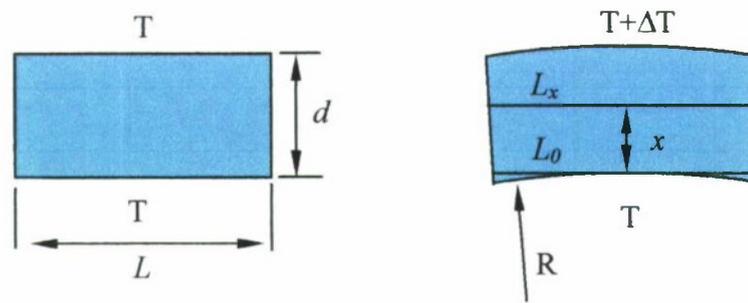
Fig. 2.3.1. Under a uniform linear temperature gradient, the crystal bar will normally curve in the arc of a circle with radius of R.

Assuming the crystal width at the cold end is L_0, then the optical length change at distance x to the cold end will be:

$$\Delta nL(x) = L_0(n_0 \cdot \alpha + \frac{dn}{dt})\Delta T(x) + L_0 \cdot \alpha \cdot \frac{dn}{dt} \cdot \Delta T(x)^2 \quad (6)$$

If the temperature is not too high, the second term on the right side of Eq. (6) will be negligible. The equation becomes:

$$\Delta nL(x) = L_0(n_0 \cdot \alpha + \frac{dn}{dt})\Delta T(x) \quad (7)$$

Here the optical length change is still proportional to the temperature change.

With an interferometer, the OPD can be precisely measured. Therefore, it is possible for us to precisely map the crystal temperature distribution by using Eq. (7). After knowing the heat flow power, the thermal conductivity then can be characterized. If the test sample is an AFB composite, the interface heat transfer coefficient can also be calculated.

1. Experimental setup

The experimental setup has been shown in Fig. 2.3.2. The test sample is placed between a heater with tunable constant power and a water cooled heat sink. The whole set up is placed inside a cryostat with vacuum environment to prevent heat convection loss with free air. At steady-state, the OPD gradient is measured by an interferometer. Two thermocouples are attached on the heater and heat sink to monitor their temperatures. In order to convert the OPD gradient to temperature gradient, the overall thermal expansion coefficient for the optical length needs to be determined first by using Eq. (3) with uniform temperature distributions.
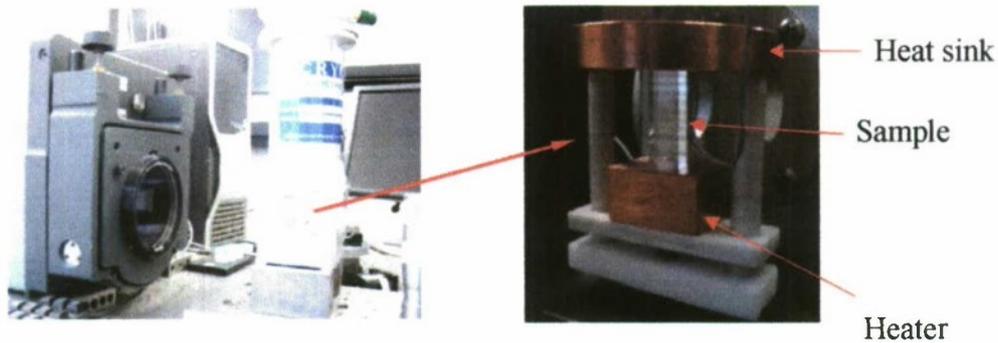
Fig. 2.3.2. Experimental setup for thermal conductivity and thermal transfer measurements.

2. Overall thermal coefficient of optical length of YAG crystal

To calibrate the system, an undoped YAG bar with dimensions listed in table 1 was fabricated and tested. Fig. 3 is the measured optical length as function of crystal temperature. The data were linearly fitted by Eq. (3). From the fitted slope, γ is determined to be 2.22×10^{-5} $°C^{-1}$ for an undoped YAG crystal. By using the already known thermal parameters of YAG crystal, we have calculated this overall thermal expansion coefficient for the YAG crystal, which is around 2.27×10^{-5} $°C^{-1}$. Our measured value is slightly smaller than the calculated value. This is because the calculation is based on the YAG parameters measured as 1064 nm. In our measurement, the interferometer has a wavelength of 1550 nm. Correspondingly, the temperature derivative of refractive index will be slightly smaller than the values at 1064 nm.
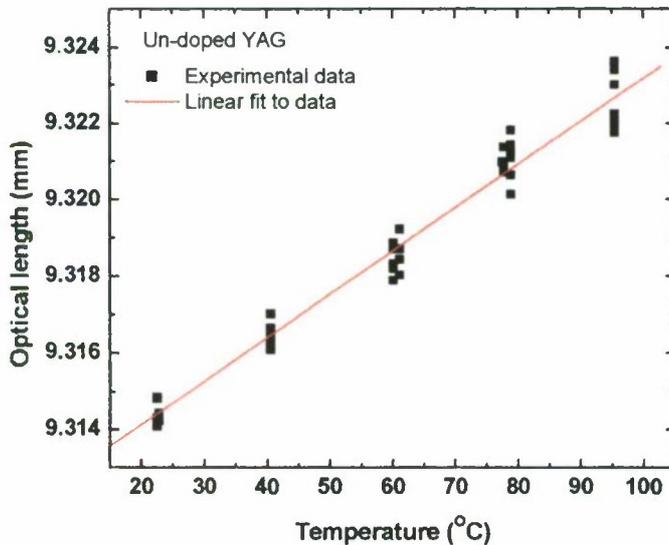

Fig. 2.3.3. Un-doped YAG optical length vs crystal temperature. The red line is a linear fit to data by using Eq. (3).

3. Thermal properties of AFB composites

The AFB composites listed in Table 1 have been investigated. The results have been plotted in Figs. 2.3.4. to 2.3.6.

Table 1. Samples and experimental results

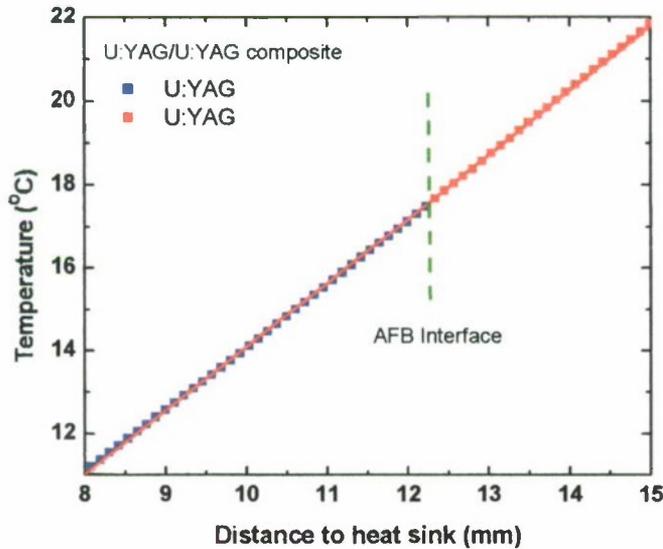| Samples	Dimensions (mm^3)	Slope	Thermal conductivity (W/cm·K)
YAG	5.09×10.10×25.02		13
U:YAG/U:YAG	5.09×10.10×25.09	1.54/1.54	13
0.6% Nd:YAG/U:YAG	5.09×10.09×24.95	0.992/0.992	13
10% Yb:YAG/U:YAG	4.65×9.72×24.99	1.40741/0.85947	7.94

Fig. 2.3.4. Temperature distribution in undoped YAG/YAG composite under heat load 1.9 W. No temperature discontinuity or heat transfer resistance can be observed at the AFB interface. The composite behaves as a single YAG crystal.
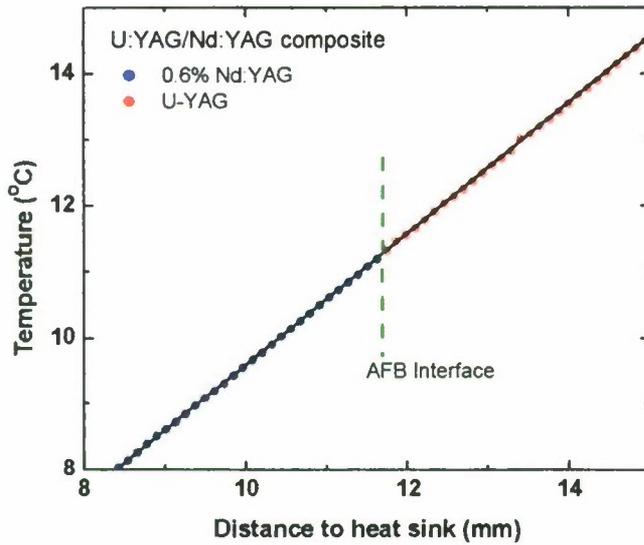
Fig. 2.3.5. Temperature distribution in 0.6% Nd:YAG/U:YAG composite for heat load of 1.24 W. The same temperature gradient on the two sides of the AFB interface indicates that the 0.6% Nd:YAG has the same thermal conductivity as un-doped YAG. No temperature discontinuity or heat transfer resistance can be observed at the AFB interface.
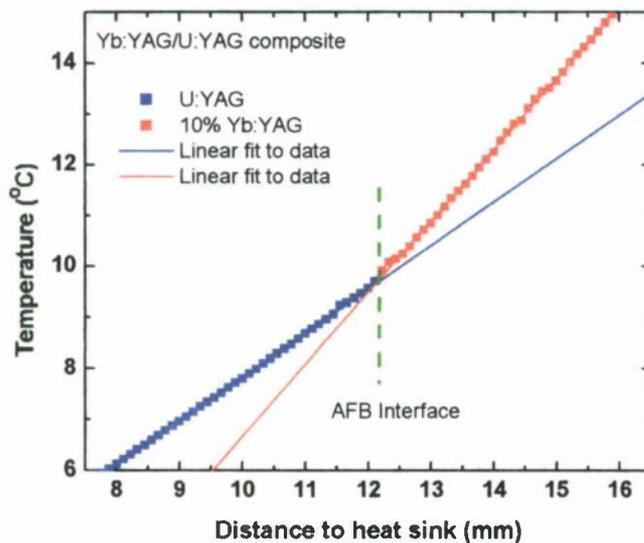

Fig. 2.3.6. Temperature distribution in 10% Yb:YAG/U:YAG composite for heat load of 1.24 W. 10% Yb:YAG has obviously larger temperature gradient than the U:YAG, which indicates a smaller thermal conductivity. No obvious temperature discontinuity can be observed at the AFB interface.

3. Laser demonstrations with AFB composites

Since composite components are primarily intended for solid state lasers, Onyx Optics has decided to increase customer confidence in the value of AFB composites by demonstrating their advantages in thermal management and high power handling by designing and building compact lasers at wavelengths of interest. The first example is a Ho:YAG laser with a demonstrated record efficiency of 81%, both cw and q-switched at an output power of 18 W and 16 W respectively. The most recent results on output power vs. repetition rates and pulse width vs. repetition rates have been reported at Advanced Solid State Photonics. Ho:YAG has uses as surgical laser, as laser illuminator propagating well in an IR transmission window and as pump laser for mid-IR tunable lasers, e.g. ZGP and Cr:ZnSe and Cr:ZnS.

3.1. High Efficiency, High Power 2.097-μm Ho:YAG Laser

3.1.1. Introduction

Ho:YAG can be resonantly pumped by 1.9-μm Thulium lasers with a low quantum defect (~9%). However, since the Holmium laser is a quasi-three level system, the laser emission suffers re-absorption loss and the output power is sensitive to the crystal temperature due to the thermal population at the laser terminal band. More importantly, the laser extraction efficiency in such quasi three-level system can only approach unity when the pump intensity is much higher than the material's saturation intensity (that is about 1.2 kW/cm^2 for Ho:YAG crystal). Therefore, in order to achieve stable and high-efficiency laser operation, high pump intensity and efficient heat removal are required. This means that, in the conventional single-pass or double-pass end-pump configuration, part of the pump energy has to be sacrificed for maintaining high enough pump intensity at the opposite end of the crystal to overcome the re-absorption loss as well as to maintain the high laser extraction efficiency. So far, most of the reported laser slope efficiencies with respect to the pump energy in Holmium doped YAG and analogous isotropic garnet crystals are around 60% [1,2]. In Ref. [3], with carefully designing of the crystal length and doping concentration, 74% slope efficiency has been reported in a double-pass end pump configuration. A slope efficiency of 82% has previously been reported in Ho:LuAG crystal, however, it is based on the absorbed pump energy [4]. In this work, by using a 4-pass end-pump design, high beam quality laser emission at 2.097 μm with M^2 ~ 1.2 has been achieved. A maximum output power of 18.6 W has been measured at a pump power of 23.7 W in a Tm:fiber laser pumped adhesive-free bonded (AFB) YAG/Ho:YAG/YAG composite. The corresponding optical-to-optical efficiency and slope efficiency are 78.5% and 81.2%, respectively. When the laser runs in Q-switched mode, the laser pulse width is found to be nearly linearly depending on the laser repetition rate. The shortest pulse width of 12.3 ns has been measured at 5 KHz.
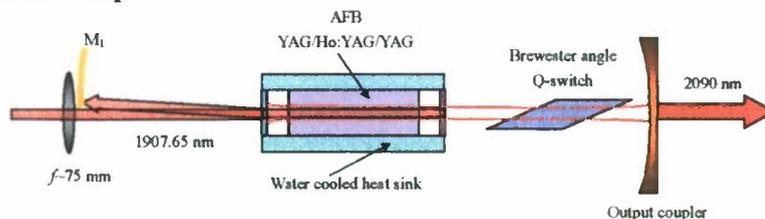
3.1.2. Experimental setup

Fig. 3.1.1. Schematic illustration of Tm:fiber 4-pass end-pumped AFB YAG/Ho:YAG/YAG laser setup.

The experimental setup is schematically shown in Fig. 3.1. The pump source is a 25-W tunable unpolarized Tm doped fiber laser at a wavelength of 1907.65 nm. The reflected pump beam will be out of the laser cavity from the pump side and then is reflected back to the crystal again by a half-round cut mirror M_1 (R~99% at pump wavelength, radius of curvature 75 mm). By such a pump arrangement, the pump laser will pass through the laser crystal 4 times.

3.1.3. Experimental results and discussions

The laser operation was achieved at both cw and Q-switched modes. The highest laser output power is measured to be 18.7 W at pump power of 24.3 W [black and green squares in Fig. 3.1.2(a)]. When the laser runs in Q-switched mode, the 60% OC was found producing the highest output power, in which case an average power of 18.6 W (or pulse energy of 1.86 mJ) was measured at a pump power of 23.7 W for a repetition rate of 10 KHz [red circles in Fig. 3.1.2(a)], corresponding to an optical-to-optical efficiency of 78.5%. From Fig. 3.1.2(a) one can see that the laser has almost identical slope efficiencies for both cw and Q-switched modes, which is measured to be 81.2%. To the best of our knowledge, they are the highest laser efficiencies ever reported in Thulium pumped Holmium lasers. We have also measured the laser output power as function of the repetition rate for fixed pump power of 21 W and plotted the results in Fig. 3.1.2(b). One can see that the laser has constant output power beyond repetition rate of 8 KHz.
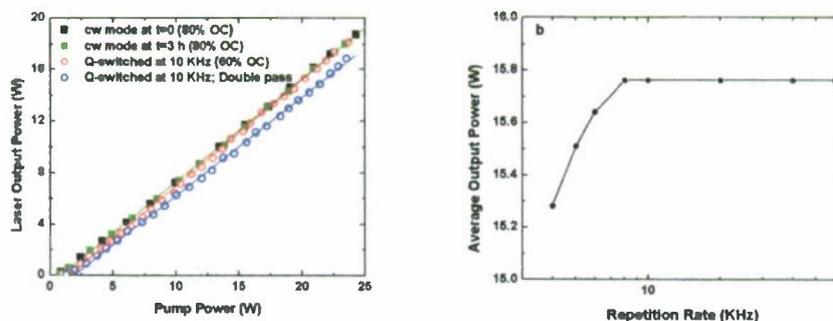

Fig. 3.1.2. (a) Laser output power vs. pump power. Black and green squires are the laser output power measured at beginning and 3 hours later for cw mode. Red and blue circles are the laser output power measured at

Q-switched mode for repetition rate of 10 KHz for 4-pass and double-pass end-pump arrangements, respectively. (b) Average laser output power as function of repetition rate for a fixed pump power of 21 W.

The laser power stability and beam quality has been reported in Ref. [5]. For a 3-hour duration the total fluctuation in the laser optical-to-optical conversion efficiency is 0.7% and the beam quality measured in our experiment is $M^2=1.2$ by using the knife-edge method.

We believe the high conversion efficiencies and stability measured in our experiment is due to the 4-pass pump configuration and the excellent heat removal capability of the AFB laser composite. In Fig. 3.1.3 we have plotted the normalized pump distribution inside the laser crystal for low pump and non-lasing conditions with $\alpha=0.91$ cm^{-1} that is the measured absorption coefficient of the laser crystal at the pump wavelength. The calculated pump wastes are 32%, 10% and 1% corresponding to single-pass, double-pass and the 4-pass arrangements, respectively. One can clearly see that the 4-pass pump arrangement can more efficiently use the pump energy meanwhile keeping the entire crystal at high pump intensity. Especially, at the non-pumped crystal end, the pump intensity is increased by a factor of 2.2. As a comparison, we have also measured the laser power dependence for a double-pass pump arrangement and plotted the results in Fig. 3.1.2(a) with blue circles. The maximum average output power and slope efficiency measured in this pump arrangement at repetition rate of 10 KHz are 16.9 W and 75%, respectively. One can see that the slope efficiency in the 4-pass arrangement is increased by about 6% compared with the double-pass pump.
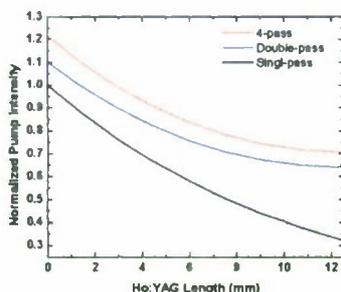

Fig. 3.1.3. Normalized pump distributions inside 1% wt Ho:YAG crystal for single-pass (black curve), double-pass (blue curve) and 4-pass (red curve) end-pump arrangements.

3.1.4. Conclusion

In conclusion, we have demonstrated high efficiency, high power 2.097-μm laser output with 4-pass end-pump design in AFB end-capped 1%wt Ho:YAG laser composite for both cw and Q-switched modes. Maximum output power of 18.6 W has been measured at pump power of 23.7 W. The corresponding laser optical-to-optical efficiency and slope efficiency are 78.5% and 81.2%, respectively. The laser slope efficiency is increased by 6% compared with double-pass pumping in the same laser composite. The shortest laser pulse width is measured to be 12.3 ns when the laser worked at Q-switch mode with repetition rate of 5 KHz. The laser has been named Hyrax.

3.1.5. References

[1] S. So, J. I. Mackenzie, D.P. Shepherd, and W.A. Clarkson, "High-power slab-based Tm:YLF laser for in-band pumping of Ho:YAG," SPIE **6871**, 68710R (2008).

[2] P. A. Budni, L. A. Pomeranz, M. L. Lemons, C. A. Miller, J. R. Mosto, and E. P. Chicklis, "Efficient mid-infrared laser using 1.9-μm-pumped Ho:YAG and ZnGeP$_2$ optical parametric oscillators," JOSA **B17**, 723-728 (2000).

[3] E. Lippert, S. Nicolas, G. Arisholm, K. Stenersen, G. Rustad, "Midinfrared laser source with high power and beam quality," Appl. Opt. **45**, 3839-3845 (2006).

[4] D. W. Hart, M. Jani, N. P. Barnes, "Room-temperature lasing of end-pumped Ho:Lu$_3$A$_{l5}$O$_{12}$," Opt. Lett. 21, 728-730 (1996).

[5] X. Mu, H. Meissner, H.-C. Lee, "Thulium fiber laser 4-pass end-pumped high efficiency 2.09-μm Ho:YAG Laser," Proc. CLEO'09, **CWH1**, Baltimore, MD (2009).

Scaling our development of high efficiency Ho:YAG lasers to a power of 300W for use as illuminator laser, Onyx Optics has designed such a system based on the demonstrated above discussed laser results.

3.2. High power, high efficiency compact 2.1-μm eye-safe illuminator laser
3.2.1. Overall Objectives
1) Design of Ho:YAG laser composites with our newly developed heat removal techniques for the master laser and laser amplifiers.
2) Design of high power (>35 W) short pulse width (~15 ns) master laser system.
3) Design of high efficiency laser amplifier system.

3.2.2. Strategy to accomplish proposed objectives
3.2.2.1. Thermal management
2.1-μm laser emission of Ho:YAG is a quasi-three-level laser system. High efficiency laser operation in such laser systems requires: 1) High in-band pump intensity to overcome the re-absorption loss and increase the laser extraction efficiency; 2) Efficient thermal management to lower the thermal population on the laser terminal band; 3) Low doping concentration to reduce nonradiative transitions. When working in the high power regime, one also needs to deal with the issues of thermal fracture limit, thermal lensing and thermal induced birefringence. The former one will set the ultimate limit for the laser output power and the later two effects can severely distort the beam qualities. Efficient thermal management will be one of the most important key elements for the success of the proposed laser system. Accordingly, AFB laser composites with new heat removal techniques that schematically are illustrated in Fig. 3.2.1 will be employed in the proposed high power laser system. The composites consist of multiple Ho:YAG segments that are sandwiched between undoped YAG crystals to increase the heat dispersion area. Moreover, the crystal length and doping concentration of each Ho:YAG segment can be modified individually to an optimized condition. In order to increase the heat dispersion

rate to the heat sink, CVD diamond wafers with thermal conductivity as high as 1800-2000 W/m·°C will be bonded outside of the composite as heat spreader wings.
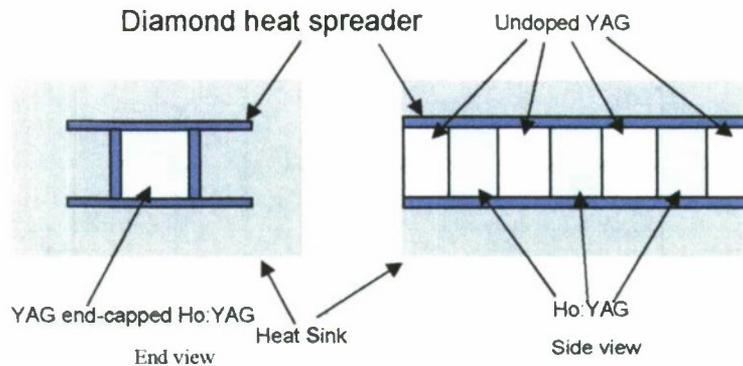

Fig. 3.2.1. Schematic ill. of high efficiency heat removal AFB laser composite.

3.2.2. Power scaling

Since most of the laser parameters of our current Hyrax laser are already a good fit with the required illumination laser system, we will first use the new designed laser composite and high power pump source to increase the Hyrax laser's average power and reduce the pulse width under conditions that do not deteriorate the laser's other parameters such as laser mode, spectral linewidth and beam quality. To further scale up the laser power, a double-pass one-stage or two-stage laser amplifier as shown in Fig. 3.2.2 will be used based on the power improvement on our current Hyrax laser system.

3.2.3. Efficiency management

In our current Hyrax laser system, a 4-pass end pumped design was employed which can efficiently maintain high pump intensity in the whole crystal length while reducing the pump waste to less than 1%. A similar end-pump design can also be used in the proposed laser amplifier to increase the amplifier efficiency as shown in Fig. 3. Currently, the wall-plug efficiency of the Hyrax laser system is mainly limited by the Tm:fiber pump laser (wall-plug efficiency ~5%). With the rapid development of long wavelength high power diode pump lasers, one can expect the system can be eventually pumped by 1.9-μm diode lasers with wall-plug efficiency close to the diode lasers wall-plug efficiency [7].
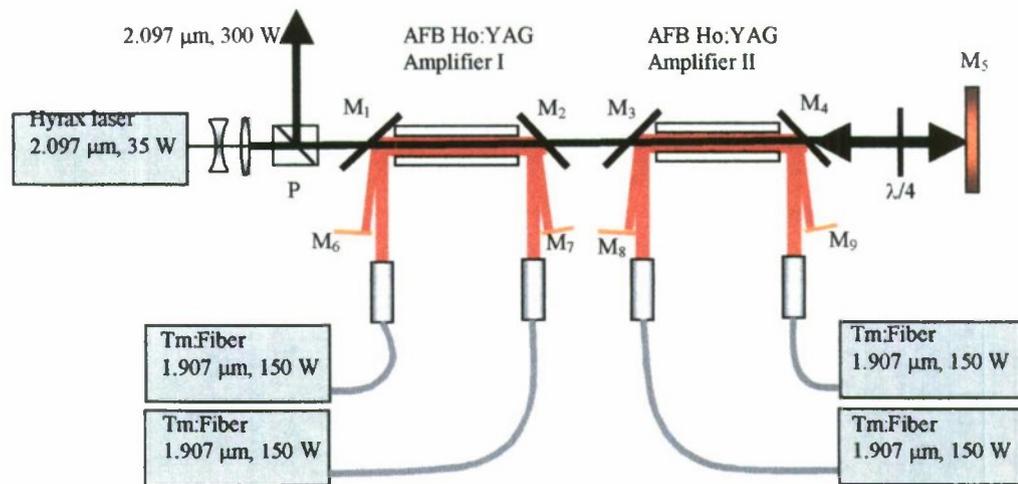
Fig. 3.2.2. Schematic illustration of the 300-W Ho:YAG laser system. Depending on the power improvement on current Hyrax laser system, a one-stage amplifier may be sufficient for reaching the 300-W average power. The whole laser oscillator-amplifier system will fit into the current Hyrax laser enclosure to maintain a compact size of 17"x7"x6".

3.2.4. Undoped end-capped laser composites

Laser composites with un-doped end caps have been demonstrated to be an efficient method to increase the stress fracture limit as well as reduce the thermal lensing effect [4-6]. In Ref. 6 for LD end pumped Nd:YAG laser rod, the highest temperature inside the pump area is found can be reduced by 35% with a 5-mm undoped YAG end cap. The thermal stress is reduced by more than 53% and the highest tensile stress center is moved from the pump surface to the barrel surface of the laser rod. For our current Hyrax laser system, we have numerically calculated the temperature and tensile stress distributions for the un-doped end capped 1at.% Ho:YAG crystal under pump power of 25 W with the 4-pass end pump configuration and compared the result with a non-composite crystal under the same pump conditions (see Fig. 3.3.3 (a)-(d)). In the calculation, we used a constant pump beam waist of 0.15 mm for the entire crystal and assumed 20% of pump power is converted to heat based on the Hyrax laser optical-to-optical conversion of 78%. The heat transfer coefficient to heat sink is assumed to be $1W/cm2\cdot°C$, which is a typical value for conductive cooling arrangement with indium interface [b]. The other parameters used in the calculation have been listed in Table 1. Even though we have used small aperture laser rod (3 mm vs. 9.5 mm in Ref. 6) for efficient management, the un-doped end caps still show the advantages by reducing both the highest temperature and tensile stress by 14%. In principle, undoped end caps have less effect on the temperature and stress easing for small aperture laser rod than the large aperture one due to the reduction of the thermal transfer in the longitudinal direction. However, for high energy laser system when large aperture laser rods are required, for example, for the second stage of power amplifier in the present proposal, the un-doped end caps will become more pronounced due to the increase of the heat transfer in the longitudinal direction.
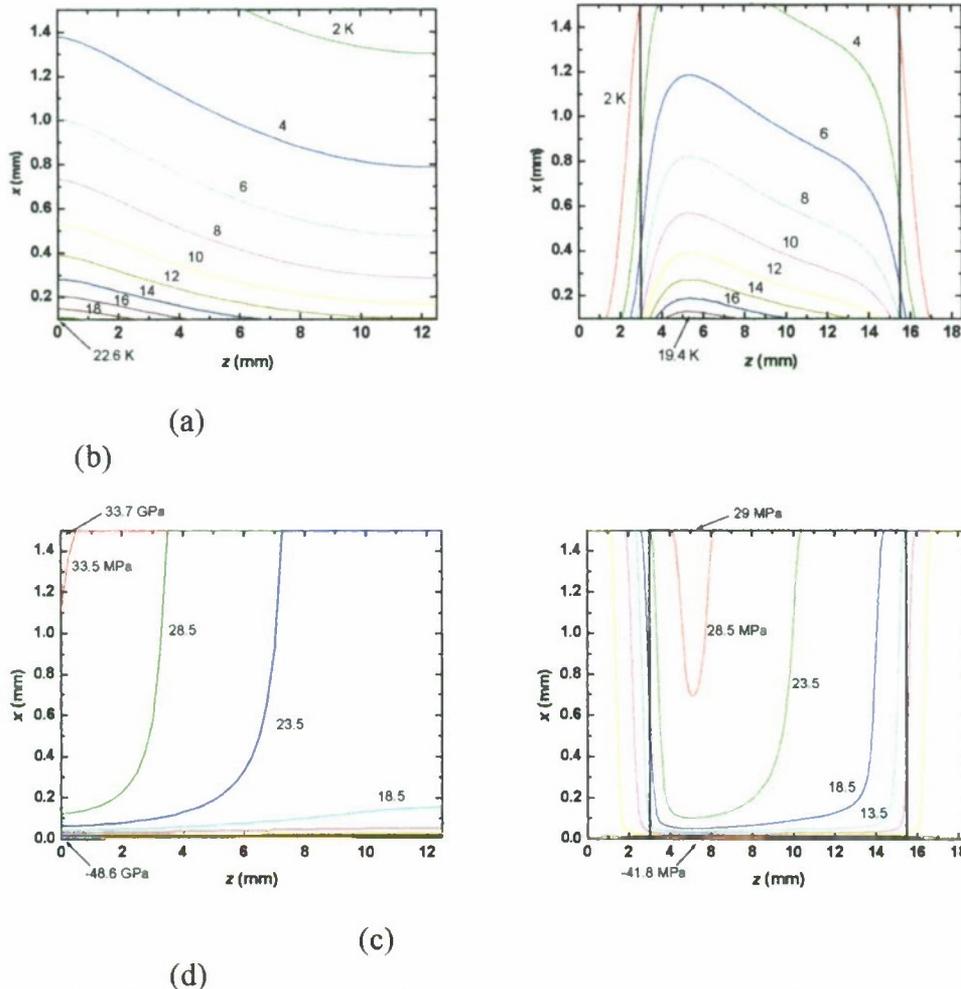
(a)

(b)

(c)

(d)

Fig. 3.3.3. Temperature and tensile stress distributions in (a, c) 12.5-mm long 1at.% Ho:YAG laser rod and (b, d) Un-doped end capped laser composite. The composite consists of a 12.5-mm long 1at.% Ho:YAG laser rod and two 3-mm long un-doped YAG ends that are adhesive-free bonded on the two ends of the doped laser rod.

Another advantage of the undoped end capped composite can almost totally erase the part of the thermal lens effect caused by the surface expansion [6]. From Fig. 3.3.3 one can see that the surfaces of un-doped caps can be efficiently cooled and have much uniformed temperature distribution than the bare ends. This can also protect the dichroic coatings on the ends of the laser crystal from the affect of thermal stress and therefore, increase their damage threshold.

3.2.5. CVD diamond heat spreader
The laser systems that conductively cooled by heat sink are more suitable for field and space applications than the liquid directly cooled system since the relaxed requirements on cooling equipments, laser coolants, and laser maintains. However, the conductive cooling has limited heat removal ability since the relatively low heat transfer coefficient

between the laser composite and the heat sink. Dependent on the contact quality, the heat transfer coefficient between the laser rod and a copper or aluminum heat sink with indium contact is typically around 1.0 W/cm^{2}K. Considering the power amplifier in the proposed MOPA could have about 90 W heat power need to be dissipated through the composites side face with an area around 1.2 cm^2, even the crystal barrel surface that directly contact with the heat sink surface could be 80 °C higher than the heat sink temperature, and the highest pump area temperature could be over 350 °C higher than the heat sink as shown in Fig. 3.3.4.
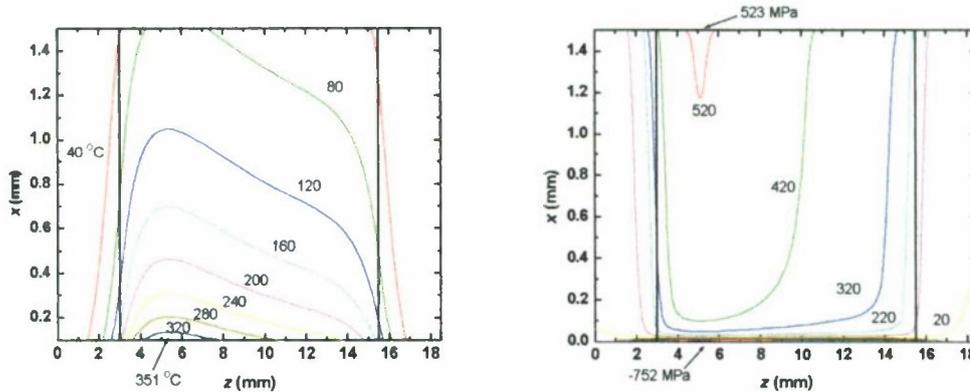

Fig. 3.3.4. Stimulated temperature distribution inside the Hyrax laser composite when it pumped by 300 W pump laser.

In the fluid cooling method, the heat transfer can be greatly increased by increasing the flow rate and pressure or change the laser crystal side surface figure. For the conductive cooling, it is lacked of efficient techniques for increasing the heat transfer coefficient besides the improvement on the contact quality. Currently, Onyx Optics is in the developing process for new heat removal techniques with our patterned AFB technology and planning to use them in the proposed high power MOPA system. One heat removal technique is using CVD diamond wafers as heat spreaders for efficient heat transfer between the laser composite and the heat sink. As illustrated in Fig. 10, the laser composite will be wrapped by four CVD diamond wafers at the four side surfaces with a large area wing structure on the top and bottom surfaces. So far 1-mm thick CVD diamond wafer with diameter of 18 mm have been commercially used in our AFB laser disks for efficient heat removal. Commonly, the CVD diamond has thermal conductivity of 1800-2000 W/m·°C that is two orders of magnitude higher than the YAG crystal and about one order of magnitude higher than the commonly used heat sink materials, such as copper and aluminum. Due to the intimate AFB contact between the laser composite and the CVD diamond, a high heat transfer coefficient can be expected at the AFB interface.
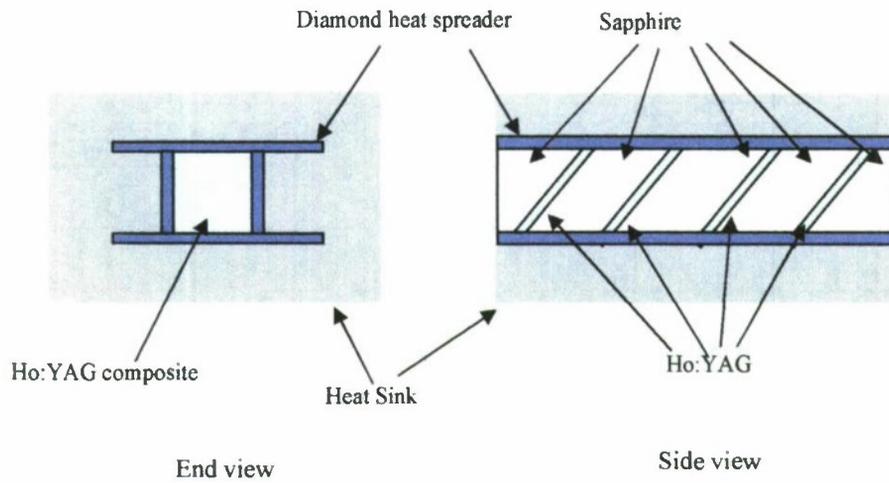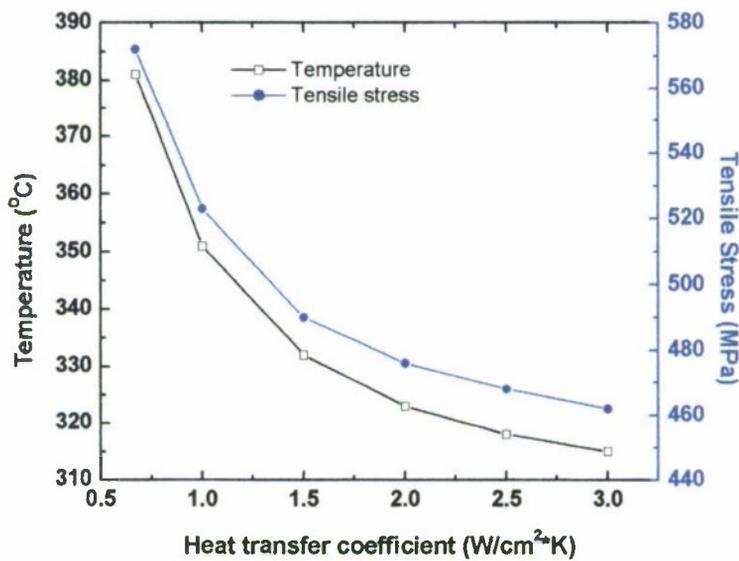
Fig. 3.3.5.

Fig. 3.3.6.

Two CVD diamond wafer will be bonded on the bottom and top side surfaces of a square laser slab as heat spreader wings. . The composites consist of multiple Ho:YAG segments that are sandwiched between undoped YAG crystals to increase the heat dispersion area. Moreover, the crystal length and doping concentration of each Ho:YAG segment can be modified individually to an optimized condition. In order to increase the heat dispersion rate to the heat sink,

3.2.6. Efficiency estimation

It is well known for efficient energy extraction from the power amplifier, the energy fluence of the input signal must be close to the saturation fluence E_{sat} of the laser material which is defined as [13]:

$$E_{sat} = \frac{h\nu}{\gamma\sigma_{em}(\lambda_l)} \quad (1)$$

Where $\gamma = 1 + \sigma_{abs}(\lambda_l)/\sigma_{em}(\lambda_l)$ for the three-level system. According to the laser parameters of Ho:YAG crystal listed in Table 1, the estimated saturation energy fluence for Ho:YAG is around 8 $J\cdot cm^{-2}$. Therefore, high beam quality, high pulse energy master oscillator will be essentially important for simplify the MOPA system and high the system efficiency.

References:

1. P. A. Budni, C. R. Ibach. S. D. Setzler, E. J. Gustafson, R. T. Castro, E. P. Chicklis, "50-mJ, Q-switched, 2.09-µm holmium laser resonantly pumped by a diode-pumped 1.9-µm thulium laser," Opt. Lett. **28**, 1016 (2003).

2. E. Lippert, S. Nicolas, G. Arisholm, K. Stenersen, G. Rustad, "Midinfrared laser source with high power and beam quality," Appl. Opt. **45**, 3839-3845 (2006).

3. S. So, J. I. Mackenzie, D. P. Shepherd, W. A. Clarkson, "High-power slab-based Tm:YLF laser for in-band pumping of Ho:YAG," SPIE **6871**, 68710R (2008).

4. Y. T. Chang, Y. P. Huang, K. W. Su, Y. F. Chen, "Comparison of thermal lensing effects between single-end and double-end diffusion-bonded Nd:YVO$_4$ crystals for $^4F_{3/2} \rightarrow ^4I_{11/2}$ and $^4F_{3/2} \rightarrow ^4I_{13/2}$ transitions ," Opt. Exp. **16**, 21155 (2008).

5. E. C. Honea, R. J. Beach, S. B. Sutton, J. A. Speth, S. C. Mitchell, J. A. Skidmore, M. A. Emanuel, S. A. Payne, "115-W Tm:YAG diode-pumped solid-state laser," IEEE J. Quantum Electron. **33**, 1592 (1997).

6. R. Weber, B. Neuenschwander, M. Mac Donald, M. B. Roos, H. P. Weber, "Cooling schemes for longitudinally diode laser-pumped Nd:YAG rods," IEEE J. Quantum Electron. **34**, 1046 (1998).

7. X. Mu, H. Meissner, H.-C. Lee, "Thulium fiber laser 4-pass end-pumped high efficiency 2.09-µm Ho:YAG laser" Proc. CLEO'09, **CWH1**, Baltimore, MD (2009).

8. J. Yu, B. C. Trieu, E. A. Modlin, U. N. Singh, M. J. Kavaya, S. Chen, Y. Bai, P. J. Petzar, M. Petros, "1 J/pulse Q-switched 2 µm solid-state laser," Opt. Lett. **31**, 462 (2006).

9. A. K. Scidharan, S. Saraf, R. L. Byer, "Yb:YAG master oscillator power amplifier for remote wind sensing," Appl. Opt. **46**, 7552 (2007).

10. M. Siebold, J. Hein, C. Wandt, S. Klingebiel, F. Krausz, S. Karsch, "High-energy, diode-pumped, nanosecond Yb:YAG MOPA system," Opt. Exp. **16**, 3674 (2008).

11. Q. Liu, X. Yan, X. Fu, M. Gong, D. Wang, "183 W TEM00 mode acoustic-optic Q-switched MOPA laser at 850 kHz," Opt. Exp. **17**, 5636 (2009).

12. C. Wandt, S. Klingebiel, M. Siebold, Z. Major, J. Hein, F. Krausz, S. Karsch, "Generation of 220 mJ nanosecond pulses at a 10 Hz repetition rate with excellent beam quality in a diode-pumped Yb:YAG MOPA system," Opt. Lett. **33**, 1111 (2008).

13. W. Koechner, Solid-state laser engineering, 5th Ed., Springer (1999).

14. K. Scholle, P. Fuhrberg, "In-band pumping of high-power Ho:YAG lasers by laser diodes at 1.9 µm," Proc. CLEO'08, **CTuAA1**, San Jose, CA (2008).

3.3. Optical Parametric Oscillations in Walk-off Compensated Adhesive-Free Bond KTP Composites

The Onyx Optics invention of quasi- noncritical phase matched nonlinear optical composites is another example of highlighting the versatility of the Adhesive-Free Bond technology where it is important for us to demonstrate the potential uses by producing devices that are superior in performance over the existing state-of-the-art, publishing on it and thereby spreading its use hopefully throughout the community. The most remarkable feature of the composite devices is the reduction of the OPO threshold by three orders of magnitude.

Quasi-noncritical phase-matched and quasi-phase-matched 2-µm optical parametric oscillations have been demonstrated and characterized in adhesive-free bonded multilayer walk-off compensated KTP composites with low pulse energy 1.064-µm pump laser.

3.3.1. Introduction

Due to the large spatial walk-off in 1.064-µm pumped 2-µm KTP optical parametric oscillations (OPO's), large-scale and high energy lasers from several millijoules to hundreds of millijoules are usually required as pump sources. In order to reduce the pump requirement in the OPO operations, one common method is using a walk-off compensated (WOC) KTP pair or pairs in the OPO operations [1-4]. In our previous work [4], we have theoretically investigated the nonlinear optical properties of adhesive-free bonded (AFB®) WOC multilayer KTP composites. We found that the multilayer composites not only can compensate the spatial walk-off, but also the phase mismatch that is caused by slight angle misalignment. The composite actually becomes quasi-noncritical phase-matched (QNCPM). In addition, based on different arrangements of the KTP orientations in the composite, quasi-phase-matching (QPM) with dual signal and idler wavelengths can also be achieved. In this work, we have successfully demonstrated the concepts of QNCPM and QPM OPO's in two 16-layer WOC KTP composites respectively with a commonly available low pulse energy Nd:YVO$_4$ laser. In the QPM KTP composite, dual signal and idler wavelengths have been obtained. Output pulse energy of 35 µJ has been achieved for the four OPO output beams at pump pulse energy of 523 µJ. For the QNCPM composite, the measured output energy is 52 µJ. The corresponding overall and slope conversion efficiencies are 9.9% and 27%, respectively.

3.3.2. Theoretical background and samples
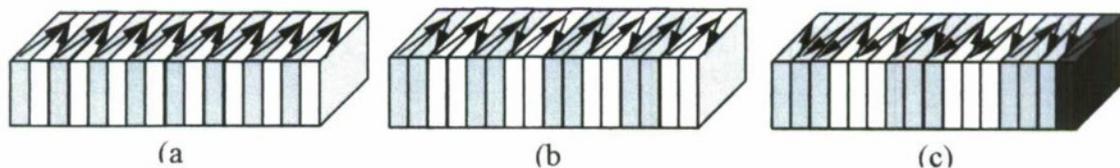

(a)   (b)   (c)

Fig. 3.3.1. KTP bonding orientation in WOC composite for (a) QNCPM OPO; (b) QPM OPO with grating period of 2 KTP layers and (c) QPM OPO with grating period of 3 KTP layers.

For a particular composite, the KTP crystals can be bonded in different orientations for WOC. One requires *z*-directions to be aligned head-to-head (or tail-to-tail) in the adjacent layers as shown in Fig. 3.3.1(a), in which all the KTP crystals have the same sign for the effective nonlinear coefficients d_{eff} and therefore, the composite has the same phase-matching condition as bulk KTP with similar features of NCPM (compensated walk-off and insensitive to slight angle misalignment) [4]. If the KTP *z*-directions are bonded head-to-tail as shown in Fig. 3.3.1(b), the effective nonlinear coefficients will have opposite signs in the adjacent crystals. The phase-matched wavelengths in the bulk KTP crystal will no longer work in this alignment because of the cancellation of the DFG field in the adjacent crystals. However, similar as in periodically poled LiNbO$_3$, KTP [5,6], QPM can be achieved when $\Delta kl = \pm\pi$, where *l* is the single crystal length used in the composite. Here one can see that the QPM WOC composite actually should have two sets of QPM wavelengths that are located at the two sides of the phase-matched wavelengths of the bulk crystal and correspond to that Δkl equals to $+\pi$ and $-\pi$, respectively [see the gray curves in Fig. 3.3.2(a)]. The KTP composite can be bonded more complicatedly as shown in Fig. 1(c) to form a QPM structure in which the sign of d_{eff} in one KTP layer is different from the other two adjacent layers [here we should notice that the adjacent bonding layers with *z*-directions head-to-head (or tail-to-tail) have the same sign for d_{eff}]. In this case, the QPM requires: $\Delta k_1 l_1 + \Delta k_2 l_2 = \pm 2\pi$ (or $\Delta kl = \pm 2/3\pi$, considering $\Delta k_1 = \Delta k_2$, *and* $l_2 = 2l_1 = 2l$). The blue curve in Fig. 3.3.2(b) is the theoretical OPO spectrum based on the QPM in the 3-layer periods. The two highest idler (or signal) output peaks correspond to the QPM condition of $\Delta kl = \pm 2/3\pi$. The second highest peaks correspond to $\Delta kl = 0$, in which only one layer is used to generate the OPO output in every three layers through the conventional CPM OPO process. The other small side peaks are due to high-order QPM.
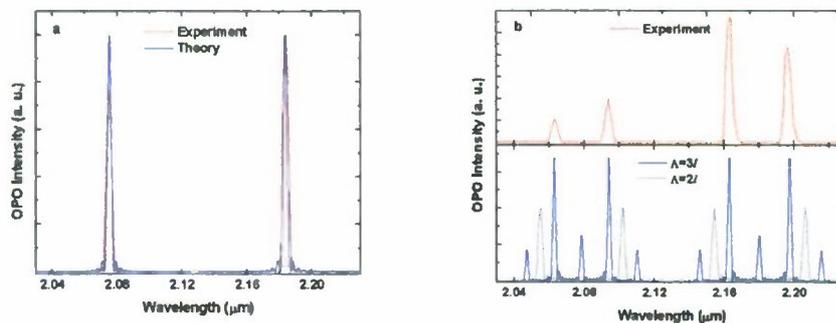

Fig. 3.3.2. Calculated and measured OPO spectrum for (a) QNCPM OPO and (b) QPM OPO. Red curves, experimental measurements; Blue and gray curves, theoretical simulations.

In order to demonstrate those concepts, two 16-layer WOC KTP samples with bonding configurations of Fig. 3.3.1(a) and Fig. 3.3.1(c) have been prepared for the QNCPM and QPM OPO experiments. The KTP single layer thickness used in the two samples both are 2 mm. The corresponding spatial walk-off in each single layer is calculated to be 94 μm for the *e*-polarized OPO wavelength, which means that a pump beam diameter as low as

94 µm can be used in those samples for fully using the crystal length. To ensure a consistent orientation and parallelism of the 2-mm KTP crystals, all the crystals used in the same composite are cut from the same large KTP disk. The original KTP disks are oriented at θ=50.2° and ϕ=0° for 1.064-µm pumped type-II KTP OPO. Each of the samples has a total length of 32 mm and clear aperture of 12.5 mm × 5 mm (5-mm edge along the y-axis) with anti-reflection (AR) coatings (R>99.7%) for both the pump and the OPO resonated wavelengths.

3.3.3. Experimental setup and results

The pump source used in the experiment is a 1.064-µm Nd:YVO$_4$ pulsed laser. The maximum pulse energy measured at the KTP surface is 523 µJ with pulse width of 15 ns at repetition rate of 1 KHz. The OPO resonator consists of two concave mirrors with radius of curvature of 50 mm and 75 mm for the pump mirror and the output coupler, respectively. The pump mirror has T=89% at 1.064 µm and R=99.5% for both signal and idler wavelengths. The output coupler (OC) has R=80% for the OPO wavelengths. The pump beam is focused on to the composite by a focus lens with f=100 mm. The pump beam waist measured inside the OPO cavity is about 110 µm.

The OPO spectra measured in our experiment for the QNCPM and QPM OPO's have been plotted in Fig. 2 (red curves in Fig. 3.3.2). One can see that those OPO wavelengths and linewidths are in good agreement with our theoretical simulations. Especially for the QPM KTP composite, as we have predicted, two closely spaced signal and idler wavelengths at 2.063, 2.094, and 2.163, 2.196 µm have been measured. (We believe that only the two strongest sets of the QPM wavelengths were oscillated in the QPM KTP composite under our experimental conditions).

The maximum output pulse energy measured for the QNCPM OPO is 52 µJ at pump pulse energy of 523 µJ. The corresponding conversion efficiency is 9.9% and the slope efficiency is around 27%, respectively. For QPM KTP OPO, the maximum OPO pulse energy is 35 µJ. The corresponding conversion efficiency is 6.7% and the slope efficiency is around 25%, respectively. From Fig. 3.3.3(a) one can see that the QNCPM OPO has the pump threshold around 250 µJ (44.6 MW/cm^2). It is worth mentioning that the conversion efficiencies measured in our experiment are quite similar to the result measured in a 20-mm long single KTP OPO in Ref. [7], in which the OPO threshold is reported about 320 mJ/pulse (~ 151 MW/cm^2) and a maximum pump energy of 636 mJ/pulse was used. In Fig. 3.3.3 we have also inserted the OPO beam profile measured by a pyroelectric camera, where one can see that no obvious beam distortion or separation can be observed even though the OPO output includes both e- and o-polarized signal and idler beams.

In Fig. 3.3.3(b) we have plotted the OPO output power as function of the incident angle in the θ direction. In both of the samples, no wavelength shift can be detected with the composite angle change. The measured angular acceptance (full-width at half-maximum) for the QNCPM and QPM OPO are 0.36° and 0.34°, respectively. One can see that they are much larger than the angular acceptance for the bulk KTP DFG, which is only 0.04° for a 32-mm KTP crystal. Similar to NCPM in a bulk crystal, the output wavelength of the QNCPM and QPM OPO's may be tuned through temperature tuning. In Fig. 3.3.3(c) and (d), we have plotted the OPO output wavelength as function of sample temperature. The wavelength shift is about 8 nm toward the degenerated direction

for all of the OPO output wavelengths when the temperature is changed from 22 °C to 222 °C.
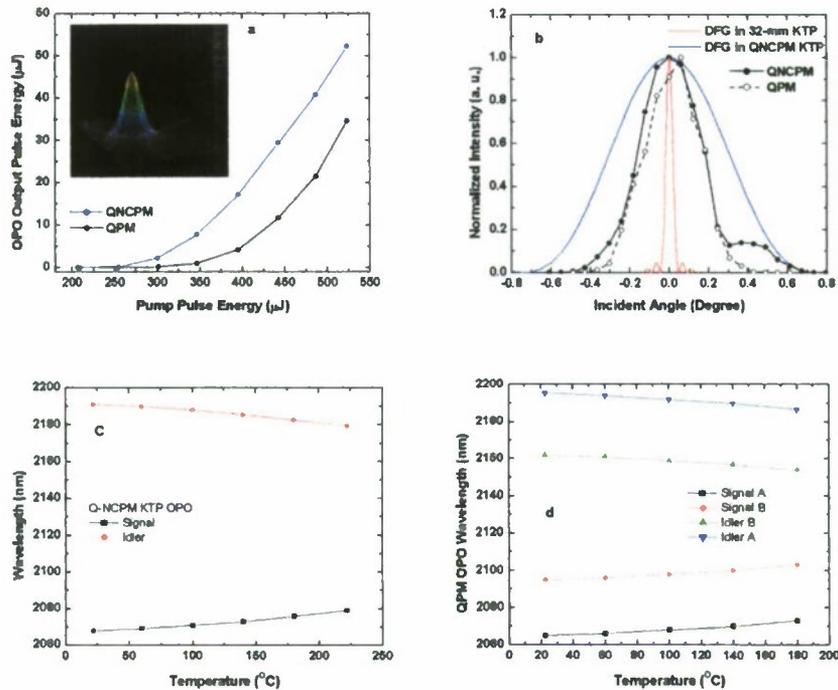

Fig. 3.3.3. (a) Output pulse energy as a function of pump pulse energy measured for QNCPM and QPM KTP OPO. The inserted figure is the output beam profile for the QNCPM OPO measured by a pyroelectric camera. (b) Normalized OPO intensity as a function of polar incident angle measured for QNCPM and QPM OPO. (c) and (d) OPO output wavelength as a function of temperature for QNCPM and QPM KTP composites, respectively.

3.3.4. Conclusion

In conclusion, high optical quality WOC KTP composites have been developed by using AFB technology. Low threshold QNCPM and QPM OPO's with compensated spatial walk-off and enhanced angular acceptance have been demonstrated. The same technology can be expected to improve the beam quality and conversion efficiency in other nonlinear materials and devices.

3.3.5. References

[1] K. Miyamoto, H. Ito, "Wavelength-agile mid-infrared (5-10 μm) generation using a galvano-controlled KTiOPO4 optical parametric oscillator," Opt. Lett. 32, 274-276 (2007).

[2] P. B. Phua, B. S. Tan, R. F. Wu, K. S. Lai, L. Chia, E. Lau, "High-average-power mid-infrared ZnGeP2 optical parametric oscillator with a wavelength-dependent polarization rotator," Opt. Lett. 31, 489-491 (2006).

[3] B. J. Perrett, P. D. Mason, D. A. Orchard, "Assessment of diffusion-bonded KTP crystals for efficient, low pulse energy conversion from 1 to 2 μm," Appl. Opt. 45, 4424-4427 (2006).

[4] X. Mu, H.-C. Lee, H. Meissner, "Walk-off corrected KTP crystal for low pulse energy pumped optical parametric oscillation," Proc. SPIE 7197, 71970G (2009).

[5] M. M. Fejer, G. A. Magel, D. H. Jundt, and R. L. Byer, "Quasi-phase-matched second harmonic generation: tuning and tolerances," IEEE J. Quantum Electron. 28, 2631-2654 (1992).

[6] A. Garashi, A. Arie, A. Skliar, G. Rosenman, "Continuous-wave optical parametric oscillator based on periodically poled KTiOPO4," Opt. Lett. 23, 1739-1741 (1998).

[7] S. Haidar, K. Miyamoto, H. Ito, "Generation of tunable mid-IR (5.5-9.3 μm) from a 2-μm pumped ZnGeP2 optical parametric oscillator," Opt. Commun. 241, 173-178 (2004).
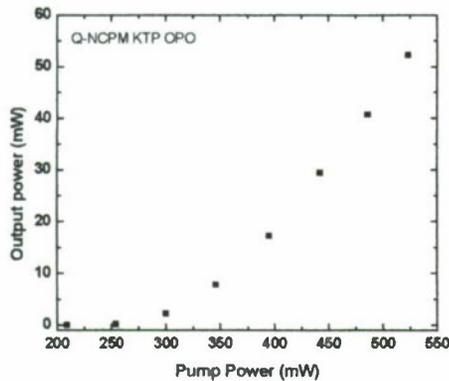
3.4. Temperature tuning of WOC KTP OPO

3.4.1. KTP OPO temperature tuning curve

As we have claimed, QNCPM and QPM KTP OPOs have enhanced angular acceptance however, as a trade off, lost angular tunability. Similar to NCPM, the output wavelength can be tuned by temperature.
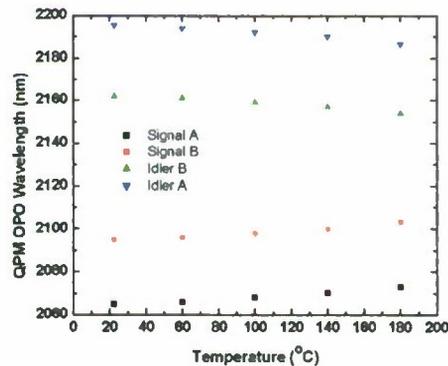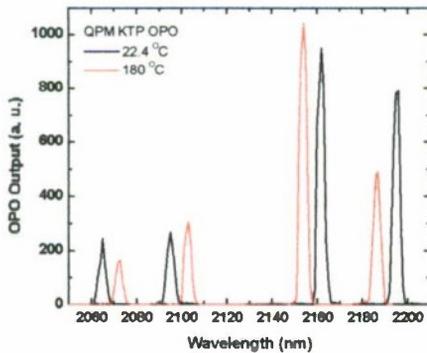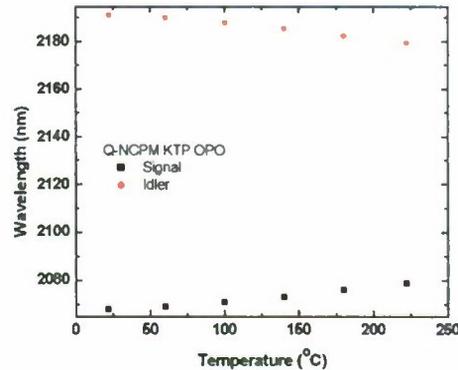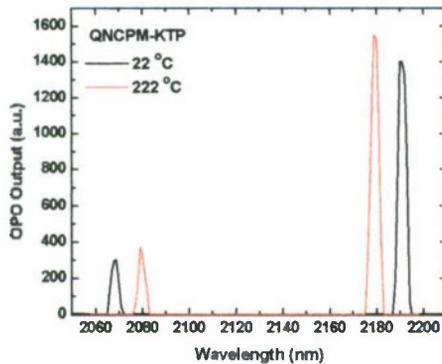
Wavelength shifts by ~8 nm when sample temperature rises from room temperature to 180 °C.

Re-measuring QNCPM KTP OPO power: 52-mW output power has been achieved at pump power of 527 mW.

3.5. ZGP OPO

3.5.1. OPO EXPERIMENTAL SETUP

Mid-IR OPO has been demonstrated with the above Ho:YAG laser system (Sec. 3.1) as pump source. The experimental setup is illustrated in Fig. 3.5.1. In order to avoid laser damaging the ZGP crystal, the pump beam from the Ho:YAG laser is focused into the ZGP crystal by a focus lens with f=250 mm and the pump power is limited to 10 W at repetition rate of 5 KHz. A dichroic beam splitter (BS) with R> 90% at 2.097 μm and T> 95% at 4.2 μm is used to separate the pump beam and the backward-going OPO output beams. Three ZGP samples from Ekspla have been tested in our OPO experiment, All the samples have dimensions of 5 mm × 6 mm × 15 mm and cutting angle of θ=55.5° for Ho:YAG pumped type-I phase-matched OPO. The two end surfaces of the samples are HR coated for wavelengths of 2.1 μm and 4.2 μm.
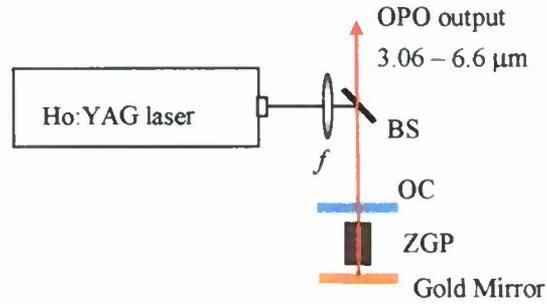
Fig. 3.5.1. Schematic illustration of ZGP OPO experimental setup.

3.5.2. Experimental results

For our current experimental setup, the OPO output wavelengths can be tuned from 3.06 – 6.6 μm in an external incident angle range of 10° (internal angle range of 3.2°, see Fig. 3.5.2. The measured output power (including both signal and idler) as function of the incident angle has been plotted in Fig. 3.5.2(b). The highest OPO output power that we have measured in our experiment is 1.44 W at the incident angle of 55.3° for pump power of 10 W. The corresponding OPO output wavelengths are at 4 μm and 4.4 μm. In Fig. 3.5.3. we have plotted the OPO output power as function of the pump power at incident angle of 55.3°. One can see that the OPO output power is linearly dependent on the power. The slope efficiency is about 16% and the OPO threshold is about 1.3 W.
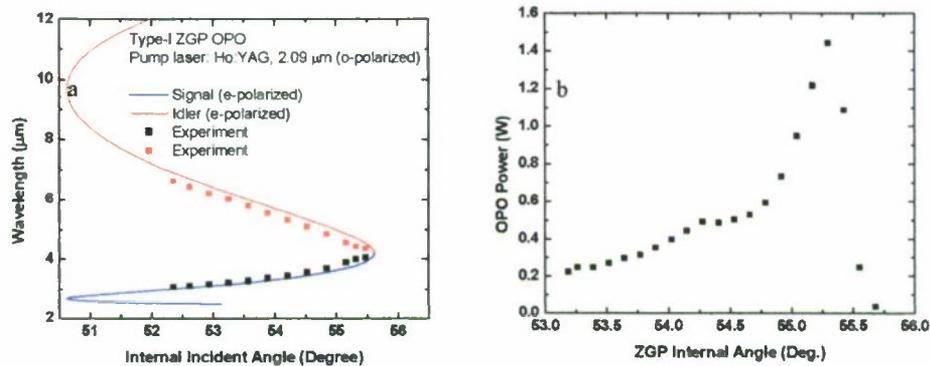

Fig. 3.5.2. (a) Comparison of experimental OPO tuning range with theory. (b) OPO output power as function of internal incident angle.
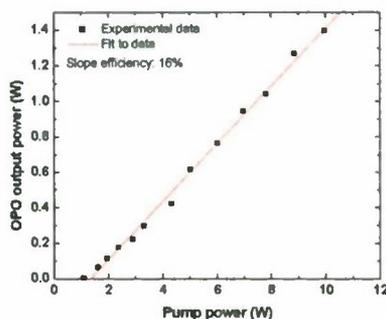
Fig. 3.5.3. ZGP OPO output power as function of pump power.

The OPO output spectrum at an internal incident angle of 55.3 and 53.2 has been measured and plotted in Fig. 3.5.4(a) and (b), respectively. One can see that the OPO output has much broader spectral line width (114 nm vs. 23 nm) at an incident angle of 55.3 than 53.2. This can be attributed to the fact that the 55.3 is close to the degeneracy
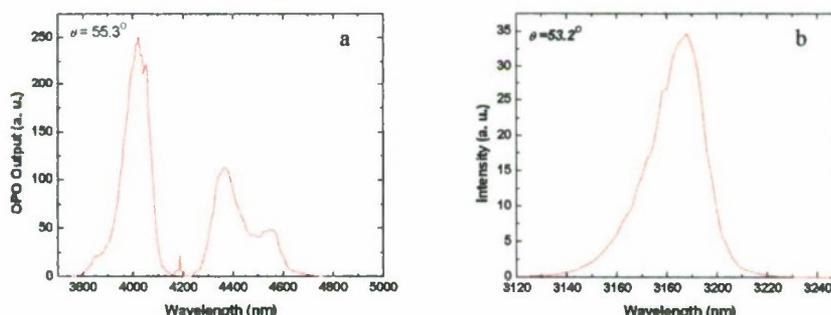
point and therefore, the OPO phase matching condition is insensitive to the output wavelength change as shown in Fig. 3.5.2(a).

Fig. 3.5.4. ZGP OPO spectrum measured at internal incident angle (a) 55.3° and (b) 53.2°.

3.5.3. Discussion

Among the three ZGP samples, the OPO operation can only be achieved in one of the three ZGP samples. The other two samples were optically damaged before the OPO operation can be reached. After checking the absorption coefficients of the three samples, we found that the sample that can be used for the OPO operation has an absorption coefficient of 0.04 cm^{-1} at the pump wavelength. The other two samples are 0.12 cm^{-1} and 0.16 cm^{-1}, respectively. Our results indicated that the high absorption coefficient of the ZGP crystal around 2 μm is the major obstacle for high efficiency mid-IR OPO generation. For future work, besides choosing low absorption loss ZGP crystals, multilayer walk-off compensated (WOC) ZGP composite will be used for further

increasing the OPO efficiency. So far, high efficiency and high beam quality 2-μm OPO has been demonstrated in multilayer WOC KTP composites [9].

3.5.4. Conclusion

High efficiency, high power 2.097-μm lasing has been demonstrated in our experiment in AFB end-capped 1%wt Ho:YAG laser composite for both cw and Q-switched modes Sec. 3.1). High slope efficiency of 81.2% and short pulse width of 11 ns have been achieved in our experiment. The laser has been successfully used as pump source for a mid-IR ZGP OPO. Tunable mid-IR wavelengths from 3.06 μm to 6.6 μm have been achieved.

REFERENCES

[1] E. Lippert, S. Nicolas, G. Arisholm, K. Stenersen, G. Rustad, "Midinfrared laser source with high power and beam quality," Appl. Opt. **45**, 3839-3845 (2006).

[2] P. A. Budni, L. A. Pomeranz, M. L. Lemons, C. A. Miller, J. R. Mosto, and E. P. Chicklis, "Efficient mid-infrared laser using 1.9-μm-pumped Ho:YAG and $ZnGeP_2$ optical parametric oscillators," JOSA **B17**, 723-728 (2000).

[3] S. So, J. I. Mackenzie, D.P. Shepherd, and W.A. Clarkson, "High-power slab-based Tm:YLF laser for in-band pumping of Ho:YAG," SPIE **6871**, 68710R (2008).

[4] D. W. Hart, M. Jani, N. P. Barnes, "Room-temperature lasing of end-pumped $Ho:Lu_3Al_5O_{12}$," Opt. Lett. **21**, 728-730 (1996).

[5] X. Mu, H. Meissner, H.-C. Lee, "Thulium fiber laser 4-pass end-pumped high efficiency 2.09-μm Ho:YAG Laser," Proc. CLEO'09, CWH1, Baltimore, MD (2009).

[6] Y. T. Chang, Y. P. Huang, K. W. Su, Y. F. Chen, "Comparison of thermal lensing effects between single-end and double-end diffusion-bonded $Nd:YVO_4$ crystals for $4F_{3/2} \rightarrow 4I_{11/2}$ and $4F_{3/2} \rightarrow 4I_{13/2}$ transitions ," Opt. Exp. **16**, 21155 (2008).

[7] E. C. Honea, R. J. Beach, S. B. Sutton, J. A. Speth, S. C. Mitchell, J. A. Skidmore, M. A. Emanuel, S. A. Payne, "115-W Tm:YAG diode-pumped solid-state laser," IEEE J. Quantum Electron. **33**, 1592 (1997).

[8] R. Weber, B. Neuenschwander, M. Mac Donald, M. B. Roos, H. P. Weber, "Cooling schemes for longitudinally diode laser-pumped Nd:YAG rods," IEEE J. Quantum Electron. **34**, 1046 (1998).

[9] X. Mu, H. Meissner, H.-C. Lee, "Adhesive-free bond quasi-noncritical phase-matched and quasi-phasematched optical parametric oscillations," Proc. SPIE 7582, 758214 (2010).

[10] X. Mu, H. Meissner, H.-C. Lee, "Optical parametric oscillations of 2 μm in multiple-layer bonded walk-off compensated KTP stacks," Opt. Lett. 35, 387 (2010).

3.6. Terahertz generation using a WOC KTP stack

This program has been undertaken in collaboration with Lehigh University, again to demonstrate the usefulness of WOC KTP

(1) Extracavity DFG

Extracavity DFG: Signal light output; idler light resonating in the cavity.
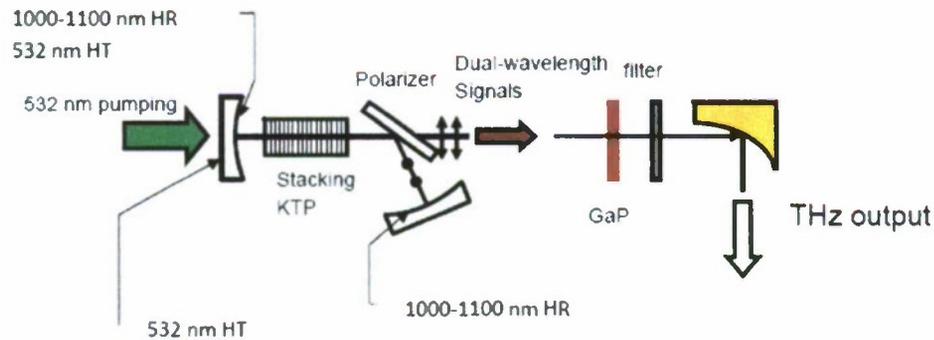
Both the input and output surfaces of Stacking KTP are coated with HT@532 nm & AR@1000-1100 nm

(2) Intracavity DFG

Extracavity DFG: idler light output; signal light resonating in the cavity.
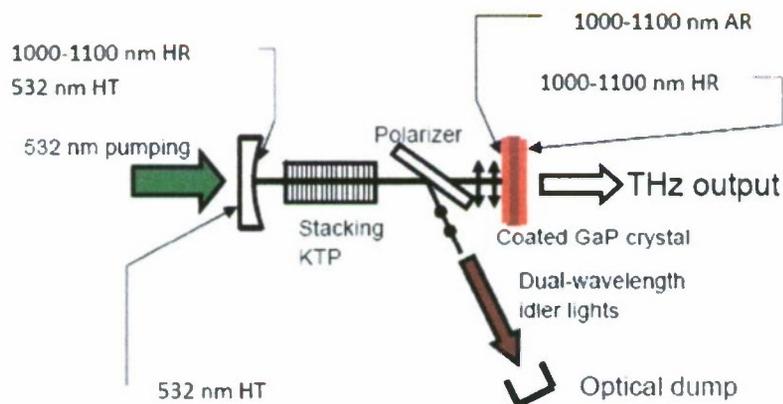
Innovative CW Yb:YAG Cryogenic Laser

Onyx Optics Inc. Subcontract # 1960221-C621

SNAKECREEKLASERS

Final Report

Prepared By:

Dr. David C. Brown, Principal Investigator
dbrown@snakecreeklasers.com

Snake Creek Lasers, LLC
RR2 Box 2753
1 Technology Drive
Hallstead, PA
18822

Phone: 570-879-4992
FAX: 570-879-0912
www.snakecreeklasers.com

Executive Summary

Substantial progress has been made in a number of areas. The highlights are summarized below:

- New crystal holders to obtain more efficient heat removal from the crystal assemblies were designed and fabricated, resulting in improved laser performance at high average power.

- We obtained close to 1 kW average power with our CW oscillator-amplifier. Corrected for unexpected coating losses in the amplifier, over 1 kW of output would have been obtained.

- Using a double-passed pre-amplifier and a single-pass power amplifier driven by a mode-locked Fianium fiber laser, we demonstrated over 700 W of ultrafast average power. Repetition rate was 50 MHz and energy/pulse about 14 μJ. Peak pulse power was 1.27 MW.

- With Jefferson National Laboratory, we demonstrated over 60 W of green output at 515 nm using un-optimized crystals and optics, and with only 160 W of fundamental average power. We expect to increase this output to 200-300 W in the near future.

- We demonstrated mode-locking in both a cryogenically-cooled Yb:YAG oscillator and a room-temperature Ti:Sapphire oscillator.

- A CW Yb:YAG cryogenically-cooled oscillator was demonstrated to have the highest slope efficiency (91.91%), the largest optical-optical efficiency (86%), and the maximum photon-photon efficiency (100%) ever demonstrated for a solid-state laser.

- Papers were prepared and submitted to laser journals for an advanced theory of heat generation in Yb:YAG lasers, absorption saturation in solid-state lasers, and for the heat-fraction limited efficient Yb:YAG cryogenic oscillator. Additional papers are in preparation for the high average power CW and ultrafast cryogenic laser systems.

- A paper summarizing the efficient Yb:YAG cryogenic oscillator results and summarizing the CW and ultrafast results was presented in June at the 23rd Annual Solid-State and Diode Laser Technology Review in Broomfield, CO.

Milestones Achieved

- Demonstration of a 1 kW CW Cryogenic Yb:YAG Laser

- Demonstration of > 100 W of Ultrafast Average Power (By 7 Times)

Most Recent Data

The following data were obtained for the high average power CW and ultrafast Yb:YAG laser systems:

CW Yb:YAG Cryogenic Oscillator-Amplifier Average Power Out vs Oscillator or Amplifier Diode Current

Yb:YAG Cryogenic Ultrafast Average Power vs Power Amplifier 940 nm Pump Power
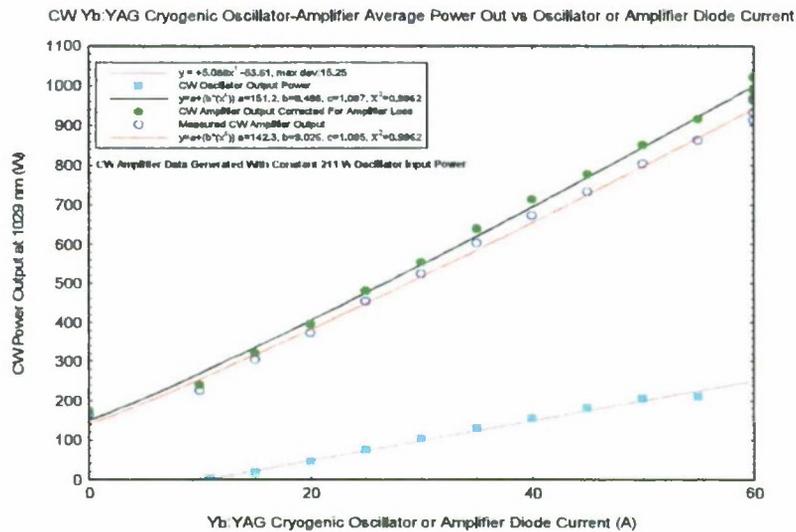
Green 515 nm Output Power vs 1029 nm Input Power

Program: Innovative CW Yb:YAG Cryogenic Laser

1. > 1 kW CW Demonstration:
1.1. Cryostat Design Improvements

1. We increased the diameter of the optical path of the aperture from 1 in to a 2 in window. The windows were AR coated for the lasing wavelength (1030 nm). (CVI model W2-PW1-2012-UV-1030-0) The base of the dewar remained similar in its overall design; the only adjustment was a widening of the window opening for the AR optics. During the initial testing of this improvement the results were beyond expectations. The output power increased from a 500 mW output with the previous design to 3.8 Watts using the new design. Tests were done using a 30 watt fiber coupled pump source.

2. Stability of the mounts was increased in six locations.

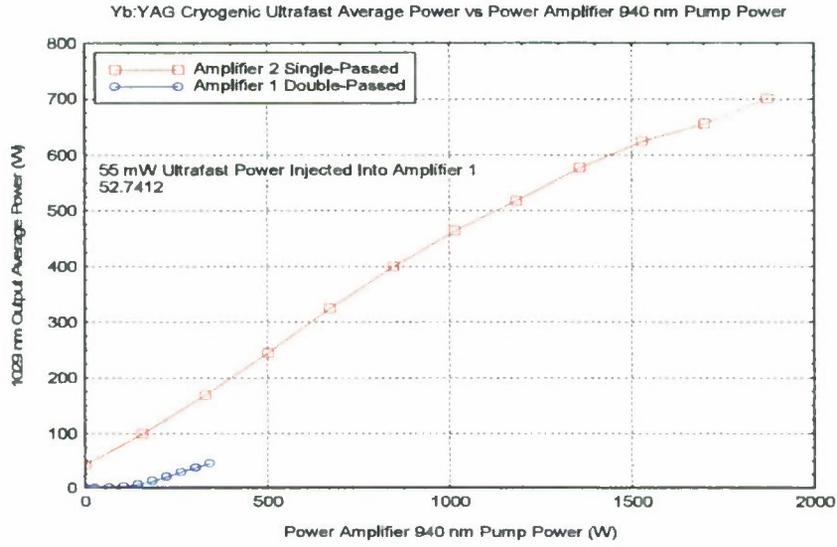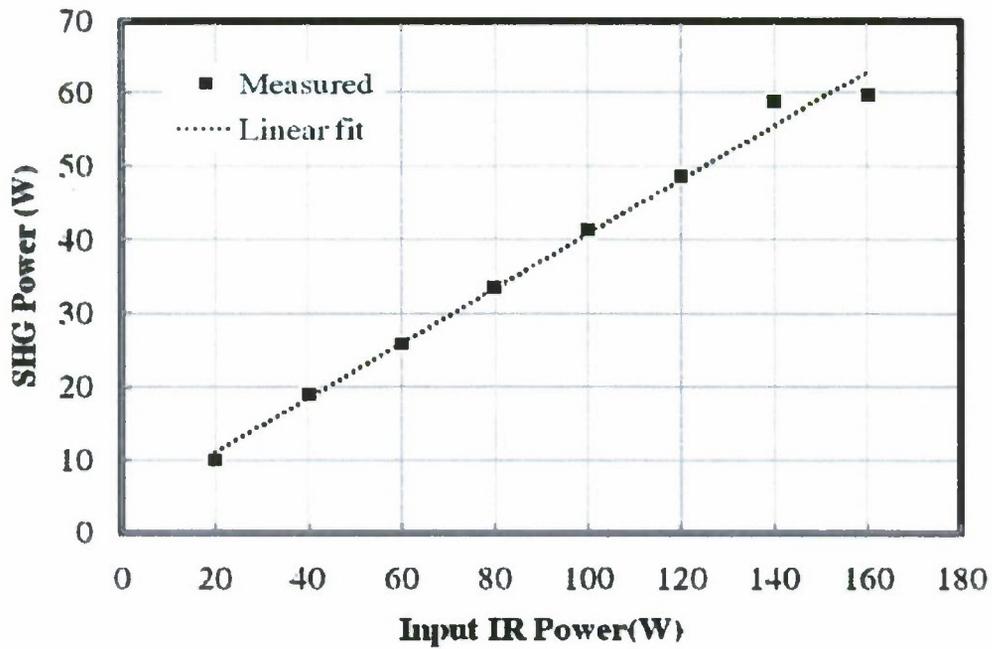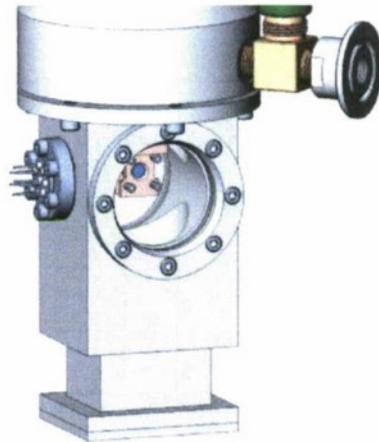3. Limitations due to the dimensions of the optical table, requires that the resonator length be decreased. To accomplish this we implemented the highest index prism commercially available that can support an intra-cavity wavelength of 1030 nm. Losses were reduced by ensuring that the apex angle provided a Brewster angle which was equal to the angle of minimum deviation.

4. To address the need for a diffraction limited source within the absorption band of the cryogenically cooled Yb:YAG crystal we went to a DPSS solution. By butt coupling a 4 watt fiber coupled single mode diode source to a Nd:YAG crystal we achieved ~500 mW of single mode output. To verify this we measured the beam profile and took an M^2 of the output. The results were excellent. With the proper focusing optics less than a 10 micron spot will be achieved. This tight focus will allow extremely low thresholds and very high slope efficiency of the system.

With the above improvements we would expect a much decreased alignment time because all optical heights are set with the custom bases. We expect a substantial improvement in the stability of the laser for achieving stable mode-locked operation over large time periods. With the improved pump source we expect increased efficiency, a lower threshold owing to the outstanding quality of the beam. Above improvements will lead to consequential improvements in the performance characteristics of the mode-locked laser.

1.2. > 1 kW CW Demonstration:

Cooling of the amplifier was identified as the major culprit in limiting the output power. In spite of significant improvements in the cooling of the amplifier, and insuring that the output was still liquid nitrogen and not a mixture of liquid and gas which is not as effective in removing heat, we continue to see a larger than expected rise in the temperature of the Yb:YAG crystals which is limiting the power output. It is likely that the cause is fluorescence and/or amplified spontaneous emission (ASE) from adjacent disks. The following typical data was taken:

Yb:YAG Cryogenic Laser CW Power Output vs Diode Current

940 nm Diode Drive Current (A)
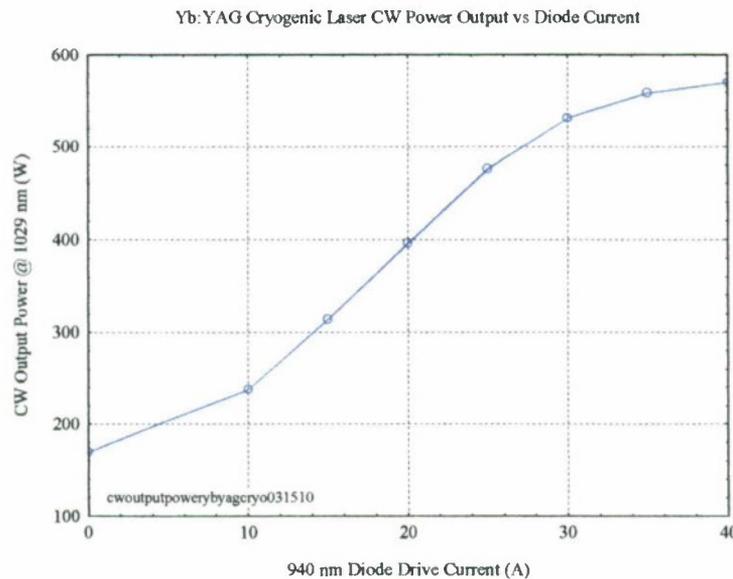
In the plot below, we show the crystal temperature measured at the top of the 1st crystal and the exit (8th crystal) of the amplifier, as well as the temperature at the location of the entrance and exit to the heat sink all crystal assemblies are mounted on. It can be seen that while there is a slight rise in temperature of the coolant after passage through the amplifier chamber, the temperature of the crystals is rising significantly faster; once above about 100 K the crystals begin to experience ground-state absorption and then "run-away" as the thermal conductivity deteriorates. Crystal 8 temperature rises above 130 °K at ~ 50 A current. The cause of the crystal heating is at present poorly understood. Previous crystal simulations show a much lower temperature rise at full pump power, so clearly an additional heating source is present. There are two likely culprits, the first heating due to impurities and the second a combination of ASE and fluorescence. We

believe the latter cause to be most likely because we believe the crystals obtained to be very high quality.
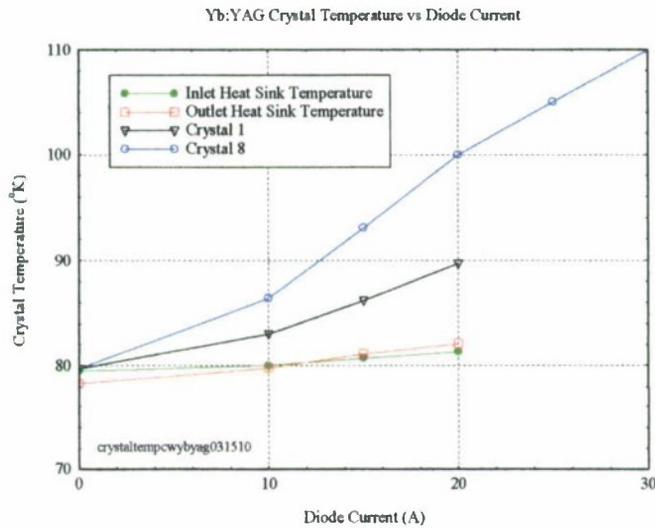
An additional problem we have identified is that the passive transmission of the amplifier is about 85%. We have traced the passive losses to about 5% loss for the entrance and exit windows and the remaining 10% to the 16 dichroic windows that seem to have deteriorated with time.

Two papers have been submitted:

Heat-Fraction-Limited CW Yb:YAG Cryogenic Solid-State Laser With 100 % Photon-Photon Efficiency

Thomas M. Bruno*, David C. Brown, and Joseph M. Singley

Snake Creek Lasers, LLC, Hallstead, PA, 18822
*Corresponding author: tbruno@snakecreeklasers.com

Submitted to Optics Express

Abstract: We report the demonstration of a heat-fraction-limited CW Yb:YAG laser operating near 77 K with output at 1029 nm, pumped with a diffraction-limited room-temperature CW Nd:YAG laser operating at 946 nm. With a 50% reflectivity outcoupler, the average threshold absorbed pump power was 18.8 mW and the average slope efficiency 91.91 %, close to the heat-fraction limited value of 91.53 %. Average optical to optical and photon to photon efficiencies are 84 % and 99.98 % respectively. To the best of our knowledge this solid-state laser is the first to operate at the heat-fraction-limit and demonstrates record slope, photon-photon, and optical-optical efficiencies for optically-pumped solid-state lasers.

References and links

1. D. C. Brown, "The Promise of Cryogenic Lasers", Invited Paper, IEEE Special Issue on Topics in Quant. Electron. 11, 587-599, May/June (2005).
2. T. Y. Fan, D. J. Ripin and R. L. Aggarwal, "Cryogenic Yb^{3+}-Doped Solid-State Lasers",
Invited Paper, IEEE J. Sel. Top. in Quant. Electron. 13, 448-459, May/June (2007).
3. P. Locovara, H. K. Choi, C. A. Wang, R. L. Aggarwal, and T. Y. Fan, "Room-Temperature Diode-Pumped Yb:YAG Laser", Opt. Lett. 16, 1089-1091 (1991).
4. D. J. Ripin, J. R. Ochoa, R. L. Aggarwal, and T. Y. Fan, "165-W Cryogenically Cooled Yb:YAG Laser", Opt. Lett. 29, 2154-2156 (2004).
5. T. Shoji, S. Tokita, J. Kawanaka, M. Fujita, and Y. Izawa, "Quantum-Defect-Limited Operation of Diode-Pumped Yb:YAG Laser at Low Temperature", J. Jour. Appl. Phys. 43, L496-L498 (2004).
6. S. Tokita, J. Kawanaka, M. Fujita, T. Kawashima, and Y. Izawa, "Sapphire-Conductive End-Cooling of High Power Cryogenic Yb:YAG Lasers", Appl. Phys. B 80, 635-638 (2005).
7. D. C. Brown, J. M. Singley, E. Yager, J. W. Kuper, B. J. Lotito, and L. L. Bennett, "Innovative High-Power CW Yb:YAG Cryogenic Laser", Proc. of SPIE, Laser Source Technology for Defense and Security IV, Ed. by M. Dubinskii and G. L. Wood, Volume 6552, Orlando, FL (2007).

Saturation Effects in CW-Pumped Solid-State Lasers
Part I: Saturated Absorption

T.M. Bruno, D.C. Brown*, and V. Vitali
Snake Creek Lasers
Hallstead, PA

Snake Creek Lasers, LLC, Hallstead, PA, 18822
*Corresponding author: dbrown@snakecreeklasers.com

Submitted to Optics Express

Abstract: Saturation effects in solid-state laser materials are important to accurately model and optimize the performance of laser devices. In this paper we present analytical and numerical results describing the absorption in CW solid-state lasers with both pump and laser saturation included, for flat-topped and Gaussian spatial distributions. Generalized absorption results are presented as a function of the ratio of pump intensity to pump saturation intensity, laser intensity to laser saturation intensity, optical thickness, and different ratios of laser to pump waists for collimated beams. These results apply to most solid-state laser energy level systems.

References and links:

1. T. M. Bruno and D. C. Brown, "Saturation Effects in CW-Pumped Solid-State Lasers Part II: Gain and Extraction Efficiency", paper to be Submitted to Optics Express
2. F. Sanchez, M. Brunel, and K. Ait-Ameur, "Pump-Saturation Effects in End-Pumped Solid-State Lasers", J. Opt. Soc. Am. B. 15, 2390-2394 (1998)
3. Y. Sato and T. Taira, "Saturation Factors of Pump Absorption in Solid-State Lasers", IEEE J. Quant. Electron. 40, 270-280 (2004)
4. O. Svelto, *Principles of Lasers*, 4th Ed., Translated by D. Hanna, Springer-Verlag (1998).
5. M. D. Feit and J. A. Fleck, Jr., "Beam Nonparaxiality, Filament Formation, and Beam Breakup in the Self-Focusing of Optical Beams", JOSA B, 5, 633-640 (1988).
6. D. J. Ripin, J. R. Ochoa, R. L. Aggarwal, and T. Y. Fan, "165-W Cryogenically Cooled Yb:YAG Laser", Opt. Lett. 29, 2154-2156 (2004).
7. D. J. Ripin, J. R. Ochoa, R. L. Aggarwal, and T. Y. Fan, "300-W Cryogenically Cooled Yb:YAG Laser", IEEE J. Quant. Electron. 41, 1274-1277 (2005).
8. D. C. Brown, "The Promise of Cryogenic Lasers", IEEE J. Selected Top. in Quant. Electron. 11, 587-599 (2005).
9. T. Y. Fan, D. J. Ripin, R. L. Aggarwal, J. R. Ochoa, B. Chann, M. Tilleman, and J. Spitzberg, "Cryogenic Yb-Doped Cryogenic Lasers", IEEE J. Selected Top. in Quant. Electron.13, 448-458 (2007).

2. High Average Power Ultrafast Demonstration:

As part of looking at heat generation in Yb:YAG lasers, we have worked out a completely new kinetics model. This work has been written up for submission to Optics Express and the abstract is shown below:

Yb:YAG Kinetics Model Including Saturation and Power Conservation

David C. Brown*
Snake Creek Lasers, LLC, Hallstead, PA, 18822
Corresponding author: dbrown@snakecreeklasers.com

Submitted to Optics Express

Abstract: We have developed a detailed kinetics model for Yb:YAG operating at any temperature and derive expressions for the heat, fluorescence, and lasing power densities and fractions, using a theoretical framework that includes conservation of ions (and power), saturation of the laser and pump beams, and a description of Boltzmann heating and cooling in the upper laser manifold. In addition, we introduce a depletion factor that allows the fluorescence and lasing fractions and power densities to be easily calculated for any ratio of the laser intensity to saturation intensity. The model is applied to Yb:YAG lasers operating at 295 and 77 °K. We find that the heat fractions at room temperature for no lasing and for complete laser saturation are significantly less than those previously reported, while at 77 °K the heat fractions are larger than at room temperature and close to previously reported values. We show for the first time to our knowledge that the efficiency of a cryogenic Yb:YAG laser operating at 77 °K will

always be greater that one operating at room temperature by almost a factor of 1.3, and that the heat fraction is not constant and varies significantly in the radial direction for Gaussian extraction beams.

References and links

1. T. Y. Fan, "Heat Generation in Nd:YAG and Yb:YAG", IEEE J. Quant. Electron. 29, 1457-1459 (1993)
2. D. C. Brown, "Heat, Fluorescence, and Stimulated-Emission Power Densities and Fractions in Nd:YAG", IEEE J. Quant. Electron. 34, 560-572 (1998).
3. A. A. Kaminskii, "Crystalline Lasers: Physical Processes and Operating Schemes", CRC Press Inc. (1996).
4. G. G. Demirkhanyan, "Intensities of Inter-Stark Transitions in YAG:Yb^{3+} Crystals", Laser Physics 16, 1054-1057 (2006).
5. Y. Sato and T. Taira, "Saturation Factors of Pump Absorption in Solid-State Lasers", IEEE J. Quant. Electron. 40, 270-280 (2004)
6. D. C. Brown and T. M. Bruno, "Saturation Effects in CW-Pumped Solid-State Lasers" paper to be Submitted to Optics Express.

3. Cryogenic Ultrafast Yb:YAG Oscillator:

A brief synopsis of our recent research activities is offered here, to place our current experiments in the proper context. In the recent past, we had conducted several experiments on room-temperature Yb:YAG in an attempt to obtain sustained modelocked lasing. We had found that using single-mode-fiber-coupled single-mode pump lasers at ~969nm, along with using confocal cavity mirrors with radii of curvature as short as 10cm, was highly beneficial to reducing the spot size of the laser mode in the Yb:YAG crystal, thus enhancing Kerr-lensing and increasing the tendency to self-modelock. We also identified critical diagnostics of the cavity stability to help us rapidly converge to the cavity parameters where Kerr-lens modelocking would be highly favored. However, we were hampered by thermal effects in obtaining and maintaining self-modelocking and/or Q-switched modelocking at room temperature. We concluded that it is necessary to return to attempting to modelock cryo-cooled Yb:YAG, employing the techniques perfected for the room-temperature experiments.

At cryogenic temperatures, the absorption peak of Yb:YAG at 969nm collapses to a narrow line, making pumping with our single-mode fiber-coupled pumps at this wavelength all but impossible. Single-mode fiber-coupled pump diodes at 940nm are currently not commercially available. We are considering using single-mode free-space-coupled single-mode pump diode chips. For now, we resorted to pumping with the previously employed wavelength of ~940nm, with a multimode fiber-coupled pump beam.

A new SCL designed cryostat was assembled as part of a separate effort of this program. This cryostat provides 3-4 hours of uninterrupted cryogenic operation before reloading of the liquid nitrogen reservoir is required. Importantly, the optical sample chamber was

significantly reduced in dimension, and the axial separation between the windows was ~7.5cm. The cryostat was pumped down to < 1 Torr pressure with a Roots blower backed by a mechanical vacuum pump, and pumping was maintained throughout the experiments. This cryostat was a significant improvement over the commercial cryostat that we have been using in our past experiments, since the latter makes it dimensionally impossible to use confocal mirrors with radii of curvature less than 15cm in our laser cavity, placing a lower limit on the laser mode spot size in the crystal.

The Yb:YAG crystal, being the same sandwiched assembly used in our previous room temperature experiments, was mounted in the cryostat, in a crystal mount which had been modified to accommodate the crossed beams of the laser cavity without aperturing. To further avoid significant aperturing, the crystal mount was offset towards the edge of the circular cold-finger, as shown in the figure on the last page, such that an X-fold confocal cavity was possible.

The laser cavity was pumped with our fiber-coupled multimode pump diode. A maximum of 16W of pump power was available from the 200 μm core diameter 0.22 NA core NA of the pump delivery fiber, at 40 A of drive current through the laser diode. After collimation of the pump beam, the shortest possible pump focusing lens was selected, to enable the tightest pump spot size (estimated to be ~100μm) in the Yb:YAG crystal. Unlike the case of room-temperature Yb:YAG, the fluorescence emitted from the crystal was masked by the much more powerful pump leakage/scatter from the crystal, and was more difficult to identify with an IR viewer. Thus, this fluorescence by itself could not be used as a means of aligning the cavity to obtain lasing. Instead, a separate 1064nm microlaser was used as an alignment tool to pre-align the cavity mirrors to make the identification of lasing convenient. The 10cm radius of curvature mirrors could be used in the setup, as shown in the figure. Several iterations of the confocal cavity fold angle were necessary to identify the rather narrow range of cavity parameters where stable lasing was obtained.

As developed in our previous experiments, the cavity mode was monitored using cameras at either end of the laser cavity. This diagnostic was critical to identifying the stability regions of the cavity where the probability of self-modelocking was the highest, manifested by the appearance of low-frequency instability of the mode profile (hopping between several modes in this case of pumping with a multimode pump). The leakage from one of the prisms was focused on a photodiode and used to diagnose pulsing behavior of the cavity and to detect modelocking. Alternatively, when we resorted to frequent repositioning of the prisms to adjust intracavity dispersion, we resorted to putting a wedge in the output beam and focusing the reflected tap beam for this diagnosis. An iris mounted on XYZ translation stage was necessary in the cavity arm without the prisms, and the iris had to be closed off to an aperture less than 1 mm (eye estimation) in order to initiate modelocking. The iris in the prism arm of the cavity, as shown in the figure, was however not as effective in yielding modelocked pulse behavior of the cavity.

We report that at 30 A of pump current, corresponding to 12.7 W ex-fiber from the pump diode, and to ~10W incident on the crystal, and with a 98% output coupler installed at the

flat reflector at the prism-end of the cavity, we observed the strong tendency of the cavity to modelock for a prism spacing of ~25 cm. This was observed over a small range of spacing of the confocal mirrors, and was more restrictive than the previous cavities using room-temperature Yb:YAG crystals, where aperturing of the beam had not been an issue.

Q-switched modelocked operation was prevalent over a ~10 cm range of prism spacings. (20-30 cm) Position of the prisms was chosen based on the peak power signal incident on the pin photo detector. While searching for the highest peak power Q-switching, the temporal density of the pulses, as seen on a one millisecond time scale, was maximized. The ideal behavior was correlated to the most appropriate prism spacing based on the highest overall activity on the oscilloscope signal. Upon optimizing the spacing of the dispersion compensating prisms, the insertion depth of the SF14 glass prisms was adjusted to maximize peak power as well as pulse density. During the iterations of adjusting the prism insertion depth the end mirrors were adjusted for maximum activity on the oscilloscope. Once the ideal insertion depth of each prism was reached the Q-switched modelocking was on the verge of CW-modelocking.

Further enhancement of these CW-modelocking characteristics occurred when a circular aperture in the cavity closed on the transverse laser mode as tightly as possible. (~100 microns) This so called 'hard aperture modelocking' proved effective. Efficacy was determined because the peak power would reach such a high value that the detector did not need to be on for the oscilloscope to receive a signal.

From this point forward the remaining portions of the alignment process were performed without the detector on. In fact this procedure acted as an excellent method of determining whether alignment was approaching a stable mode-locking position. At this point the only remaining parameter to optimize was the cavity length. The arm which did not contain the prisms was considerably shorter, therefore adding length would only increase the cavity stability. By rotating the end mirror, while pulling it back along the propagation axis, the optimal length was found for modelocking behavior. After translating the about .5 cm along the propagation axis the CW-modelocking regime was found. To gain an understanding of how long the stability range was the mirror was pulled back further until CW-modelocking was lost. The range turned out to be ~ .75 cm. Once at the location of optimal CW-modelocking the end mirrors and prisms were adjusted to maximize stability. The CW-modelocking sustained itself though the Kerr lensing process over a large period of time and started immediately after the pump was turned off then on again. Overall intensity fluctuations took place on a 1ms time scale due to instabilities in the mounts. Once this vibrational source of instability is found the overall fluctuations will cease.

3.1. Experimental results on Cryogenic Ultrafast Yb:YAG Oscillator:

We placed the present highly-doped Yb:YAG crystal into the dewar and began cryogenic ultrafast laser experiments. In order to improve stability we have experimentally investigated the CW power output with a view towards further understanding thermal effects, which are now playing no important role. We expanded the dewar window size to

allow us the ability to get the short focal length resonator mirrors close to the Yb:YAG crystal to achieve a small spot size. We also replaced the high power 940 nm fiber-coupled diodes with SCL manufactured 946 nm diode-pumped solid-state lasers. These lasers have now been finished, improved, and fully characterized, and we have now achieved impressive results in the CW mode. By matching the diffraction-limited pump beam to the resonator mode and with careful alignment, we have obtained the highest slope, optical-optical, and photon efficiencies ever recorded for a solid-state laser. Updated output vs absorbed power data are shown in the Figure below, followed by a plot of the optical-optical efficiency:
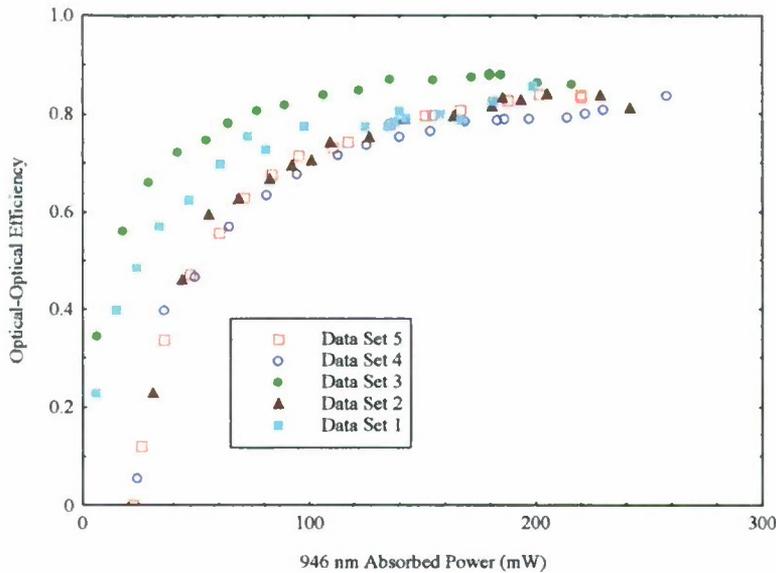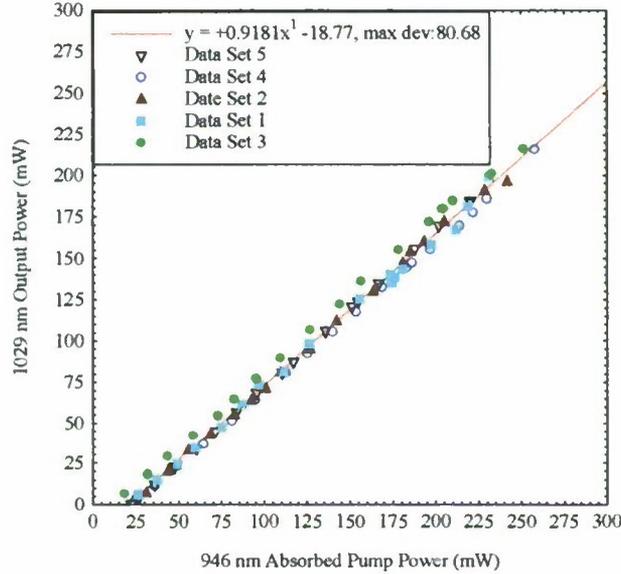
As may be seen from the Figures, which shows measured power vs absorbed 946 nm pump power, five separate sets of CW data were taken.

We have used the Fianium fiber laser to generate over 250 W of average power. The repetition rate was 50 MHz so the energy/pulse was over 5 μJ. The measured pulsewidth of about 10 psec gives a peak power per pulse of about 500 kW.

An average output power of 236 W was achieved by using a single 1m F.L. PCX lens to collimate the output of the Fianium oscillator into the first amplifier and a single 75 cm F.L. PCX lens to collimate the output of the first amplifier into the second amplifier. At full output power the beam had a Gaussian spatial profile with an M^2 value of 1.28. The pulse width at full power was 8.88 ps and the pulse-to-pulse stability was 2.1%.

The previous CW MOPA configuration of the cryogenically-cooled Yb:YAG laser system was converted to an ultrafast two-stage amplifier configuration for the purpose of conducting a series of ultrafast pulse amplification experiments described here. The main goal of this series of experiments was to determine the configuration that produced the highest average output power while maintaining excellent beam quality, pulse shape, and pulse-to-pulse stability.

The Fianium (Model FM1030) 1030 nm, 10 ps, 10 nJ fiber laser with an average output power of 100 mW and a repetition rate of 50 MHz was first directed through a pair of Electro-Optics Technology, Inc. isolators (Model numbers 04-00574 and 08-00708) that provide a combined 60 dB of isolation from the amplifier stages. The output of the Fianium laser was then bore sighted into the first amplifier stage with a pair of high-reflecting mirrors while a 1 meter focal length lens collimated the beam. The first amplifier stage consisted of 7 10-at% cryogenically-cooled Yb:YAG crystal assemblies that were each pumped by opposing ~30 W 940-nm diodes from LIMO. We discovered that two of these diode sources failed during this series of experiments. The output of the first amplifier stage was then bore sighted with a pair of high-reflecting mirrors while a 0.75 meter focal length lens was used to collimate the beam. The second amplifier stage consisted of 8 10-at% cryogenically-cooled Yb:YAG crystal assemblies that were each pumped by opposing ~100 W 940-nm diodes from LIMO. The output of the second amplifier stage was directed at a highly-reflective mirror (R @ 1030 nm ~99.99%) that was then steered towards another highly-reflective concave mirror (R @ 1030nm ~99.9%, ROC = -60 cm) that was used to expand the beam into the Coherent water-cooled 1 kW power meter head. The 0.01% leakage from the first mirror, after the output of the second amplifier stage, was used to make beam quality, temporal, spectral, and pulse stability measurements. The figure below shows the experimental set up.
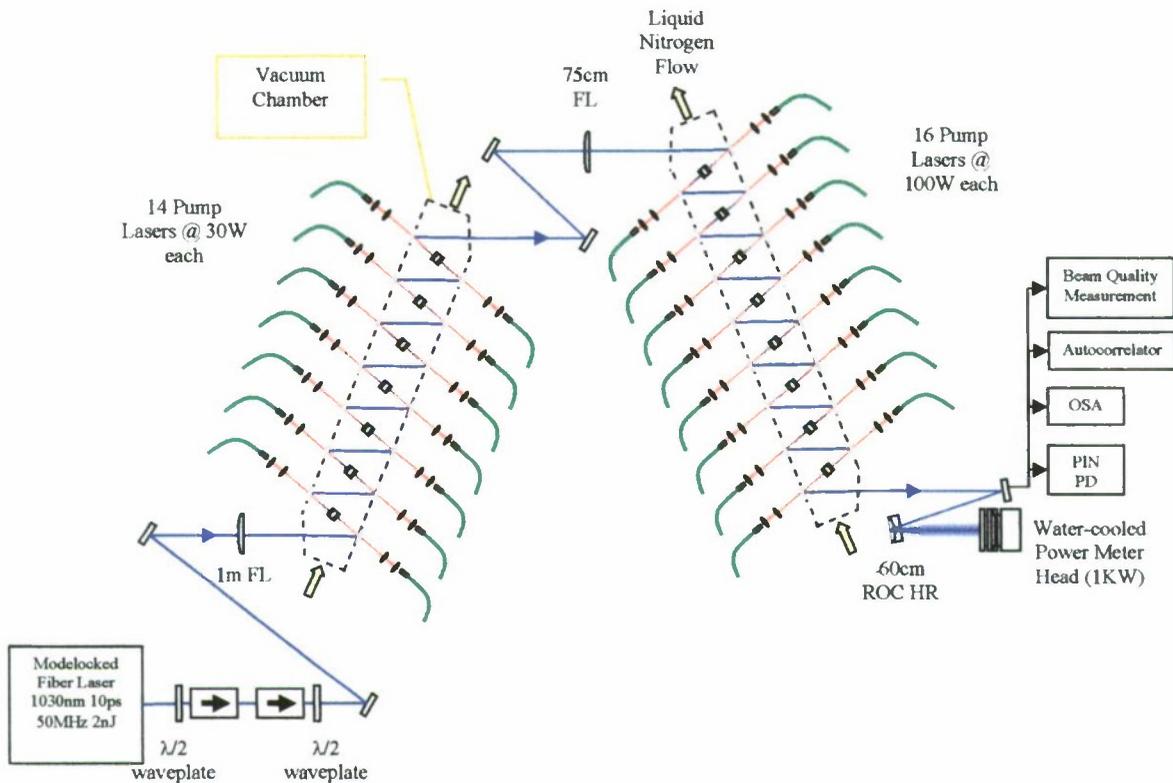
Experimental set up of the 1030 nm ultrafast seed laser, 1st amplifier stage, 2nd amplifier stage, and beam characterization equipment.

4. Ti:Sapphire Laser Oscillator, Pre-Amplifier, and Stretcher and Compressor:
4.1. Ti:Sapphire Datasheet

A very important part of completing a Ti:Sapphire oscillator and system design is to collect into one place all of the relevant data needed so that the system performs as expected. Snake Creek Lasers has been collecting such data for quite some time for a number of different laser materials, creating detailed datasheets of the properties, and is almost finished with Ti:Sapphire. We have received a sample and have generated our own room-temperature digitized absorption data using our high-resolution Shimadzu UV-VIS-NIR (SolidSpec-3700/3700DUV) spectrophotometer. We are currently installing a cryo dewar in the spectrophotometer and expect to generate data for Ti:Sapphire at 77 K shortly. The room temperature cross-section data are shown below for both the pi and sigma transitions:

Ti:Sapphire Absorption Cross-Section as a Function of Wavelength (nm)
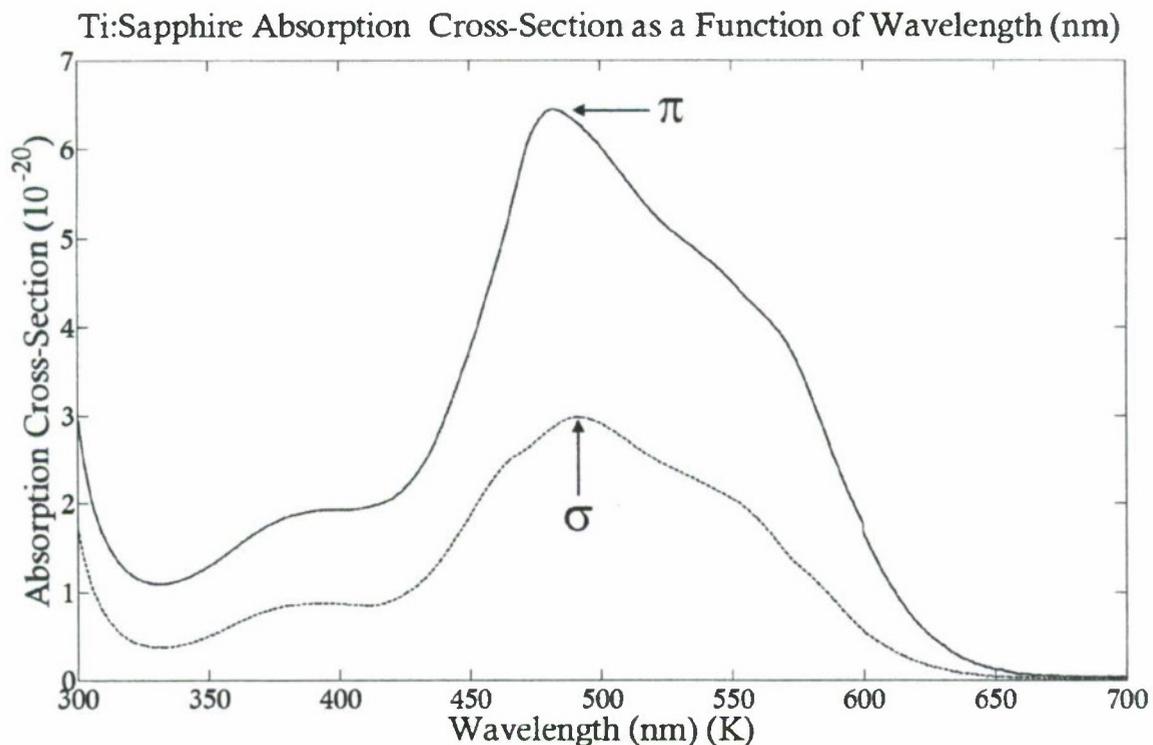
We noticed a significant departure of our data from that originally published by Moulton; our cross-sections were considerably more intense. As a consequence we scaled our data to the Moulton data temporarily. After we have obtained good cryogenic data we will send the sample to Northern Analytical for a more precise calibration of the doping density and then re-calculate the cross-sections and compare them to Moulton.

4.2. Ti:Sapphire Absorption Experiments and Modeling:
To obtain a detailed understanding of how well pump power will be converted into usable laser energy we began by observing the absorption properties. A thorough understanding of the changes in absorption as a function of pump power would influence the crystal length, doping density, focal spot size as well as whether a retro-reflected pump configuration would be in order.

4.3. Ti: Sapphire Crystal Length Optimization:
The purpose of the Crystal length optimization problem is to find the ideal length crystal that would provide the lowest threshold, highest slope efficiency while simultaneously giving stable performance.

4.4. Pump Absorption Modeling:
We are developing a model for pump absorption in the Ti:Sapphire laser, including pump saturation. We have found a solution to this problem for a spatially flat-topped beam in the form of a transcendental equation that can be solved numerically.

We have finished our pump absorption modeling including saturation and for flat-top and Gaussian pump and extraction profiles. These results have been extended to cover both four level and quasi-three-level kinetics systems, and are being written up for publication. The model will be used to optimize absorption in Ti:Sapphire oscillator and in designing the Ti:Sapphire ultrafast system, as well as more detailed modeling of Yb:YAG lasers. In order to better understand Yb:YAG laser operation, we are working towards building a systems level kinetics code that includes the effects of saturation of the pump and laser beams. This code will be able to propagate beams through CW laser systems and accurately calculate the gain and extraction efficiency. We have almost finished the preparation of a paper, the first of two-parts, that will also be submitted to Optics Express.

4.5. Ti:Sapphire Oscillator Crystal Designs
The Jade 2 Nd:YLF green laser was delivered and was installed by a Thales technical person. A considerable amount of work went into identifying the following parts for the Ti:Sapphire system:

- Broadband Faraday Rotator
- Broadband Pulse Picker
- Broadband Flat Laser Mirrors
- Broadband Polarizers

The Ti:Sapphire oscillator is now operating in CW mode. We have been improving the design and started mode-locking experiments.

Accounting of all Federal funds expended during the term of the Agreement

Invoice #	Date	Invoice Amount	Total Amount Invoiced
Invoice 1	05/16/2007	62,803.00	62,803.00
Invoice 2	06/25/2007	107,999.00	170802.00
Invoice 3	07/24/2007	188,726.00	359528.00
Invoice 4	08/22/2007	81,201.00	440729.00
Invoice 5	09/27/2007	171,614.00	612343.00
Invoice 6	10/26/2007	134,406.00	746749.00
Invoice 7	11/21/2007	93,787.00	840536.00
Invoice 8	12/29/2007	85,939.00	926475.00
Invoice 9	01/23/2008	93,186.00	1019661.00
Invoice 10	02/23/2008	83,942.00	1103603.00
Invoice 11	04/01/2008	115,174.00	1218777.00
Invoice 12	04/30/2008	101,223.00	1320000.00
Invoice 13	07/21/2008	144,119.00	1464119.00
Invoice 14	08/20/2008	109,672.00	1573791.00
Invoice 15	09/18/2008	104,118.00	1677909.00
Invoice 16	10/28/2008	199,443.00	1877352.00
Invoice 17	11/25/2008	122,320.00	1999672.00
Invoice 18	12/22/2008	106,765.00	2106437.00
Invoice 19	01/27/2009	127,418.00	2233855.00
Invoice 20	03/02/2009	115,282.00	2349137.00
Invoice 21	03/25/2009	138,012.00	2487149.00
Invoice 22	04/23/2009	116,468.00	2603617.00
Invoice 23	05/26/2009	86,940.00	2690557.00
Invoice 24	06/18/2009	287,084.00	2977641.00
Invoice 25	07/29/2009	202,329.00	3179970.00
Invoice 26	08/25/2009	137,169.00	3317139.00
Invoice 27	09/22/2009	180,412.00	3497551.00
Invoice 28	10/26/2009	176,130.00	3673681.00
Invoice 29	11/20/2009	180,416.00	3854097.00
Invoice 30	12/30/2009	194,443.00	4048540.00
Invoice 31	01/20/2010	132,823.00	4181363.00
Invoice 32	02/22/2010	119,069.00	4300432.00
Invoice 33	04/12/2010	127,518.00	4427950.00
Invoice 34	04/26/2010	133,050.00	4561000.00
Invoice 35	07/19/2010	100,000.00	**4661000.00**